

1 **Performance of AIRS ozone retrieval over the central Himalayas: Case studies of biomass**
2 **burning, downward ozone transport and radiative forcing using long-term observations**

3

4

5 Prajwal Rawat^{1,5}, Manish Naja¹, Evan Fishbein², Pradeep K. Thapliyal³, Rajesh Kumar⁴, Piyush
6 Bhardwaj⁴, Aditya Jaiswal¹, Sugriva N. Tiwari⁵, Sethuraman Venkataramani⁶, Shyam Lal⁶

7

8

9

10 ¹ Aryabhata Research Institute of Observational Sciences (ARIES), Nainital, 263001, India

11 ² NASA Jet Propulsion Laboratory, Pasadena, CA 91109, USA

12 ³ Space Applications Centre, ISRO, Ahmedabad 380015, India

13 ⁴ National Center for Atmospheric Research (NCAR) Boulder, CO 80307, USA

14 ⁵ DDU Gorakhpur University, Gorakhpur 273009, India

15 ⁶ Physical Research Laboratory (PRL), Ahmedabad, 380009, India

16

17

18

19

20 **Corresponding author:** Manish Naja (manish@aries.res.in)

21

22

23

24

25

26 **Short Summary:**

27 Satellite based ozone observations have gained wide importance due to their global coverage.
28 However, satellite retrieved products are indirect and need to be validated, particularly over ~~the~~
29 ~~complex terrain regions mountains~~. Here, ozonesondes launched from a Himalayan site are
30 utilized to assess the ~~Atmospheric Infrared Sounder (AIRS)~~ ozone retrieval. AIRS is shown to
31 overestimate ozone in the upper troposphere and lower stratosphere, while the differences with
32 ozonesonde are lower in the middle troposphere and middle stratosphere.

33
34
35
36
37
38
39
40
41
42
43
44
45
46
47
48
49
50

51 **Abstract**

52 Data from 242 ozonesondes launched from ARIES Nainital (29.40° N, 79.50° E, and 1793 m
53 elevation) are used to evaluate the Atmospheric Infrared Sounder (AIRS) version 6 ozone profiles
54 and total column ozone during the period 2011-2017 over the central Himalaya. The AIRS ozone
55 products are analyzed in terms of retrieval sensitivity, retrieval biases/errors, and ability to retrieve
56 the natural variability of columnar ozone, which has not been done so far from the Himalayan
57 region having complex topography. For a direct comparison, averaging kernels information is used
58 to account for the sensitivity difference between the AIRS and ozonesonde data. We show that
59 AIRS has lower differences with ozonesonde in the lower and middle troposphere and stratosphere
60 with nominal underestimations of less than 20%. However, in the upper troposphere and lower
61 stratosphere (UTLS), we observe a considerable overestimation of the magnitude, as high as 102%.
62 The weighted statistical error analysis of AIRS ozone shows higher positive bias and standard
63 deviation in the upper troposphere of about 65% and 25%, respectively. Similar to AIRS, Infrared
64 Atmospheric Sounding Interferometer (IASI) and Cross-track Infrared Sounder (CrIS) are also
65 able to produce ozone peak altitudes and gradients successfully. However, the statistical errors are
66 again higher in the UTLS region that are likely related to larger variability of ozone, lower ozone
67 partial pressure and inadequate retrieval information on the surface parameters. Furthermore,
68 AIRS fails to capture the monthly variation of the total ozone column, with a strong bimodal
69 variation, unlike unimodal variation seen in ozonesonde and Ozone Monitoring Instrument (OMI).
70 In contrast, the UTLS and the tropospheric ozone columns are in reasonable agreement. Increases
71 in the ozone values by 5 - 20% after biomass burning and during events of downward transport
72 are captured well by AIRS. Ozone radiative forcing (RF) derived from total column ozone using
73 ozonesondes data ($4.86 \text{ mW/m}^2\text{mWm}^{-2}$) matches well with OMI ($4.04 \text{ mW/m}^2\text{mWm}^{-2}$), while
74 significant RF underestimation is seen in AIRS ($2.96 \text{ mW/m}^2\text{mWm}^{-2}$). The fragile and complex
75 landscapes of the Himalayas are more sensitive to global climate change and establishing such
76 biases and error analysis of space-borne sensors will help study the long-term trends and estimate
77 accurate radiative budgets.

78
79
80
81

82 **1. Introduction**

83 Atmospheric ozone is an essential trace gas that plays a crucial role in the atmospheric oxidizing
84 chemistry, air quality, and earth’s radiative budget. The stratospheric ozone absorbs harmful solar
85 ultraviolet radiation and protects biological life on earth, whereas tropospheric ozone, being a
86 secondary air pollutant (Logan et al., 1985; Pitts and Pitts, 1997; Pierce et al., 2009; Monks et al.,
87 2015; Lelieveld et al., 2018) and greenhouse gas, contributes to global warming and can harm
88 human health and crops when present in higher concentrations near the surface (Fishman et al.,
89 1979; Ebi and McGregor 2008; Lal et al., 2017). Different radiative forcing of ozone from the
90 stratosphere (cooling) to the troposphere (heating) (Lacis et al., 1990; [Wang et al., 1993](#); Forster
91 et al., 2007; ~~[Wang et al., 1993](#)~~; Hegglin et al., 2015) demonstrate its potential importance as an
92 atmospheric climate gas (Shindell et al., 2012; Thornhill et al., 2021). Hence, information
93 regarding precise long-term variability in global ozone distribution is vital for better characterizing
94 atmospheric chemistry and global climate changes (McPeters et al., 1994; Kim et al., 1996; Myhre
95 et al., 2017).

96
97 In recent decades, observations of ozone from space-borne sensors (microwave limb sounding,
98 UV-VIS, and IR) have become an increasingly robust tool for global and higher temporal
99 monitoring (Fishman et al., 1986; Munro et al., 1998; Bhartia et al., 1996; Foret et al., 2014). This
100 increases our ability to analyze various influences of human activities on the atmospheric chemical
101 composition, including ozone, study their long-term impact on climate (Fishman et al., 1987; Fry
102 et al., 2012; Tarasick et al., 2019; Thornhill et al., 2021), and estimate reliable radiative budgets
103 (Hauglustaine and Brasseur 2001; Gauss et al., 2003; Aghedo et al., 2011). However, the space-
104 based sensors are indirect and measure the atmospheric composition based upon specific

105 algorithms utilizing radiative transfer models and a-priori information. Hence, the retrieval outputs
106 need to be evaluated with certain reference instruments for establishing the credibility and better
107 utilization of space-borne data.

108
109 The Himalayas, a complex terrain region, has the largest abundance of ice sheets outside polar
110 regions that impacts global/regional radiative budgets and climate pervasively (e.g., Lawrence and
111 Lelieveld, 2010; Cristofanelli et al., 2014; Zhang et al., 2015). Very sparse in-situ and ground-
112 based observations in this region, along with inadequate information on the surface parameters,
113 makes it difficult to retrieve atmospheric composition from space-borne instruments. This is
114 because the ozone weighting function, a measure of the retrieval sensitivity and a fundamental
115 retrieval component, depends upon various atmospheric parameters like surface temperature,
116 surface emissivity, and terrain height (Rodgers et al., 1976, 1990; Bai et al., 2014), which is not
117 uniform over the foot-print size of the AIRS (~ 13 km x 13 km) over the Himalayas. Usually, the
118 ozone weighting function has a shorter integrating path over the elevated terrain regions, which
119 follows a smaller weighting function and provides lesser sensitivity and higher errors in the final
120 retrievals (Coheur et al., 2005; Bai et al., 2014).

121
122 The Atmospheric Infrared Sounder (AIRS) onboard the Aqua satellite has been providing reliable
123 vertical profiles of ozone, temperature, water vapor, and other trace gases globally twice a day
124 since 2002. Numerous validation studies of AIRS retrieved ozone have been carried out for
125 different versions since it started operating (2002). For example, Bian et al. (2007) studied AIRS
126 version 4 over Beijing and discussed the potential agreements (within 10%) between AIRS and
127 ozonesonde (GPSO3) ozone, particularly in the upper troposphere and lower stratosphere (UTLS)

128 region with the capability of AIRS to identify various Stratosphere-Troposphere Exchange (STE)
129 and transient convective events. Similarly, a study over Boulder and Lauder by Monahan et al.
130 (2007) using a similar AIRS version showed despite the larger biases in the lower and middle
131 tropospheric region, the retrieval algorithm captures the ozone variability very effectively with a
132 positive correlation of more than 70%. However, that study suggested a need for tropopause-
133 adjusted coordinates in the a-priori profiles. Both these studies (Bian et al., 2007; Monahan et al.,
134 2007) show larger biases in AIRS ozone in the lower and middle tropospheric regions; however,
135 shifts in retrieval biases and errors were seen towards the UTLS region in version 5 (Divakarla et
136 al., 2008), apart from significant improvements in the lower troposphere. The retrieval
137 methodology has also changed significantly between V4 and V5. Version 4 or earlier used
138 regression retrieval as the first guess in physical retrieval, while later versions used a climatology-
139 based first guess for the physical retrieval based on other works (McPeters et al., 2007). Also,
140 radiative transfer models, selected channel sets, and clarified quality indicators have been modified
141 and improved in all successive versions.

142
143 The AIRS ozone retrieval in V5 has improved significantly with retrieval biases and root mean
144 square error (RMSE) less than 5% and 20%, respectively (Divakarla et al., 2008), over the tropical
145 regions. However, there is not much discussion and studies of the assessment for AIRS ozone over
146 the Himalayas' complex terrain, where retrieval is expected to be erroneous due to large surface
147 variability within its footprint. Also, most of the previous studies (Bian et al., 2007; Divakarla et
148 al., 2008; Pittman et al., 2009) did not utilize the averaging kernels information of the AIRS that
149 is vital for satellite evaluation.

150

151 Here, the evaluation of AIRS version 6, which entirely depends upon the infra-red (IR)
152 observations after the failure of the AMSU sensor, is presented in terms of statistical analysis and
153 ability to retrieve the natural variability of ozone at various altitudes over the central Himalayan
154 region using in-situ ozonesonde observations convolved with AIRS averaging kernels.
155 Additionally, the present study assessed the AIRS retrieval algorithm using IASI and CrIS radiance
156 information for one year. AIRS columnar ozone (i.e., total, UTLS, and tropospheric columns) is
157 also assessed with ozonesonde, OMI, and Microwave Limb Sounder (MLS) observations. AIRS
158 has a long-term data set for ozone and meteorological parameters, establishing such biases and
159 error analysis is essential to make meaningful use of its data to characterize the Himalayan
160 atmosphere, study the trends, radiative budgets, perform the model evaluation and data
161 assimilation over this region.

162

163 **2 Data and Methodology**

164 **2.1 Data Description**

165 **2.1.1 AIRS**

166 Atmospheric Infrared Sounder (AIRS) onboard Aqua satellite, in the sun synchronous polar orbit
167 at 705 km altitude, is a hyperspectral thermal infrared grating spectrometer with equatorial
168 crossings at ~13:30 local time (LT). It is a nadir scanning sensor that was deployed in orbit on
169 May 4, 2002. AIRS, along with its partner microwave instrument, the Advanced Microwave
170 Sounding Unit (AMSU-A), represents the most advanced atmospheric sounding system placed in
171 space using cutting-edge infrared and microwave technologies. These instruments together
172 observe the global energy cycles, water cycles, climate variations, and greenhouse gases, however,
173 after AMSU failure, the retrieval now mostly depends upon the AIRS IR observations. The AIRS

174 infrared spectrometer acquires 2378 spectral samples at resolutions ($\lambda/\Delta\lambda$) ranging from 1086 to
175 1570 cm^{-1} , in three bands: $3.74\text{ }\mu\text{m}$ to $4.61\text{ }\mu\text{m}$, $6.20\text{ }\mu\text{m}$ to $8.22\text{ }\mu\text{m}$, and $8.8\text{ }\mu\text{m}$ to $15.4\text{ }\mu\text{m}$
176 (Fishbein et al., 2003; Pagano et al., 2003). The independent channels of AIRS permit retrieval of
177 various atmospheric states and constituents depending upon their corresponding spectral response,
178 even in the presence of a 90% cloud fraction (Susskind et al., 2003; Maddy and Barnet, 2008). In
179 this study, we have used Level 2 Support physical products of AIRS (AIRS2SUP). The AIRS2SUP
180 files (~240 granules/day) possess extra information over the standard AIRS files, e.g., information
181 on averaging kernel and degree of freedom, including vertical profiles at 100 pressure levels,
182 against just 28 in the standard product.

183

184 The support product profiles contain 100 levels between 1100 and 0.016 mbar. While it has a
185 higher vertical resolution, the vertical information content is no greater than the standard product.
186 The information on averaging kernels and degree of freedoms (DOFs) is utilized to understand the
187 retrieved products more comprehensively. The DOFs of ozone, a measure of significant eigen
188 functions used in the AIRS retrieval, have an average value of 1.36 over the tropical latitude band
189 (Maddy and Barnet 2008) (Table S1), while over the balloon collocated region, an average DOFs
190 of 1.62 is observed (Figure S1). In the present study, the AIRS data is flagged as best quality when
191 the cloud fraction is less than 80%, and the degrees of freedom (DOF) are greater than 0.04.
192 However, analysis of cloud fraction over our collocated region shows (Figure S2) only 7% of
193 observations during 2011 - 2017 had a cloud fraction of more than 80%.

194

195

196

197 **2.1.2 IASI (NOAA/CLASS)**

198 The Infrared Atmospheric Sounding Interferometer (IASI) onboard MetOp satellites, with a
199 primary focus on meteorology than climate and atmospheric chemistry monitoring, is a nadir
200 viewing Michelson interferometer (Clerbaux et al., 2007). The first MetOp satellite was launched
201 in October 2006 (MetOp-A), and IASI was declared operational in July 2007. MetOp is a polar
202 sun-synchronous satellite having descend and ascend nodes at 09:30 and 21:30 LT, respectively.
203 IASI measures in the IR part of the EM spectrum at a horizontal resolution of 12 km at nadir up to
204 40 km over a swath width of about 2,200 km. IASI covers an infra-red spectral range between 3.7
205 to 15.4 μm with a total of 8461 spectral channels, out of which 53 channels around 9.6 μm are
206 utilized for ozone retrieval. IASI level 2 ozone products provided by NOAA National
207 Environmental Satellite Data and Information Service (NESDIS) Center for Satellite Application
208 and Research (STAR) are used in this study. The IASI (NOAA/CLASS) ozone product is retrieved
209 based on the AIRS algorithm and has various quality control flags (Table S2). Only QC=0 data
210 which represents a successful IR ozone retrieval, is used.

211

212 **2.1.3 CrIS/ATMS (NUCAPS)**

213 The Cross-track Infrared Sounder (CrIS) and Advanced Technology Microwave Sounder (ATMS)
214 onboard the Suomi NPP satellite were launched in 2011 to feature the high spectral-resolution
215 (“hyperspectral”) observations of earth’s atmosphere. The CrIS instrument is an advanced Fourier
216 transform spectrometer with an ascending node 13:30 LT and flies at a mean altitude of 824 km
217 and performs fourteen orbits per day. It measures high-resolution IR spectra in the spectral range
218 650 - 2550 cm^{-1} with a total of 1305 channels. The ATMS is a microwave sounder with a total of
219 22 channels ranging from 23 to 183 GHz. These two instruments, CrIS and ATMS, operate in an

220 overlapping field-of-view (FOV) formation, with ATMS FOVs re-sampled to match the location
221 and size of the 3×3 CrIS FOVs for retrieval under clear to partly cloudy conditions. Here the
222 NUCAPS algorithm-based ozone product of CrIS is utilized. The NOAA Unique CrIS/ATMS
223 Processing System (NUCAPS) is a heritage algorithm developed by the STAR team based on the
224 AIRS retrieval algorithm (Susskind et al., 2003, 2006). The NOAA implemented NUCAPS
225 algorithm is a modular architecture that was specifically designed to be compatible with multiple
226 instruments. The same retrieval algorithms are currently used to process the AIRS/AMSU suite
227 (operations since 2002), the IASI/AMSU/MHS suite (operational since 2008), and now the
228 CrIS/ATMS suite (approved for operations in January 2013). Here again, various quality controls
229 for retrieved data are provided by the NUCAPS science algorithm team, and we used QC=0 for
230 lesser discrepancies in our evaluation (Table S2). These research products follow a similar retrieval
231 algorithm as developed by the AIRS science team, which gives us further opportunity to assess the
232 AIRS retrieval algorithm for IASI and CrIS radiances.

233

234 **2.1.4 Ozonesonde**

235 ~~Electrochemical~~[EN-SCI electrochemical](#) concentration cell (ECC) ozonesondes and GPS-
236 radiosondes ([iMet](#)) have been launched from the Aryabhata Research Institute of Observational
237 Sciences (ARIES) (29.4° N, 79.5° E, and 1793 m elevation) Nainital (Figure 1), a high-altitude site
238 in central Himalaya, since 2011 (Ojha et al., 2014; Rawat et al., 2020), the only facility in the
239 Himalayan region having regular launchings. ECC ozonesonde relies on the oxidation reaction of
240 ozone with potassium iodide (KI) solution (Komhyr et al., 1967, 1995) to measure ozone partial
241 pressure in the ambient atmosphere. The typical vertical resolution of ozonesonde is about 100 -
242 150 m and has a precision of better than ± 3 - 5 % with an accuracy of about ± 5 - 10 % up to 30

243 km altitude under standard operating procedures (Smit et al., 2007); [Smit & ASOPOS Panel,](#)
244 [2020](#)). The ozonesonde is connected to iMet-radiosonde via a V7 electronic interface, where
245 radiosonde consists of GPS, PTU, and a transmitter to transmit signals to the ground. ~~Due~~[The](#)
246 [ozonesonde sensor's successful performance is assured before launch \(about 3 - 7 days before](#)
247 [launch\) as part of advance preparation and during the day of launch by maintaining and reviewing](#)
248 [the records for background current, pump flow rate, response time, etc. The ozonesonde data](#)
249 [quality is further assured by estimating these ECC ozonesondes' total ozone normalization factor](#)
250 [with collocated OMI total ozone. These factors are well within the ASOPOS recommendation with](#)
251 [an average of \$1.0 \pm 0.04\$, which implies the reasonable quality of these ozonesondes \(Smit &](#)
252 [ASOPOS Panel, 2020\). Additionally, ozonesonde observations from present site have also been](#)
253 [utilized in SUSKAT \(Bhardwaj et al., 2018\) and StratoClim \(Brunamonti et al., 2018\) field](#)
254 [campaigns and in other studies \(Ojha et al., 2014\). Further, owing](#) to higher accuracy and in-situ
255 measurement, ozonesonde has been widely used worldwide for satellite and model validation
256 (Divakarla et al., 2008; Nassar et al., 2008; Monahan et al., 2007; Kumar et al., 2012a, 2012b;
257 Dufour et al., 2012; Verstraeten et al., 2013; Boynard et al., 2016; Rawat et al., 2020). Both the
258 ascending and descending data were recorded by ozonesonde, however, due to time lag in
259 descending records, only ascending data is utilized (Lal et al., 2013, 2014; Ojha et al., 2014). The
260 data is collected at the interval of about 10 meters which is averaged over 100 meters interval using
261 a 3σ filter that removes the outlier values (Srivastava et al., 2015; Naja et al., 2016).

262

263 **2.1.5 Other Auxiliary Data**

264 Additionally, collocated and concurrent OMI and MLS observations are also used to study the
265 tropospheric ozone, UTLS, and total ozone column due to their reasonable sensitivity and well-

266 validated retrievals (Veefkind et al., 2006; Ziemke et al., 2006; Fadnavis et al., 2014; Wang et al.,
267 2021). The tropospheric ozone column obtained from OMI and MLS is based on the residual
268 method, which depends upon the collocated difference between the MLS stratospheric ozone
269 column and OMI total ozone column, which is described in detail by Ziemke et al. (2006).
270 Furthermore, the MLS version 4 data is utilized for the UTLS column above 261 hPa due to its
271 credibility in this range for scientific applications (Livesey et al., 2013; Schwartz et al., 2015).
272 Moreover, for fair statistical analysis between ozonesonde and MLS ozone profile, Gaussian
273 smoothing is applied to ozonesonde with full width at half maximum equal to typical upper
274 tropospheric vertical resolution (~ 2 - 4 km) of MLS (Livesey et al., 2013). The best quality data
275 of MLS with data flags, i.e., status=even, quality > 0.6, and convergence < 1.18, is utilized (Ziemke
276 et al., 1998; Barre et al., 2012). However, a slightly different collocation criterion of 3°×3° grid
277 box and daytime collocation is utilized for MLS in this work due to coarser resolution and to get
278 sufficient matchups.

279

280 **2.2 Methods of Analysis**

281 The balloon launch time is mostly around 12:00 IST (Indian Standard Time, which is 5.5 hours
282 ahead of GMT). The Aqua satellite comes over the India around 1:30 pm and 1:30 am IST. Hence
283 for collocation, only noontime (ascending) data (or ± 3 hours of balloon launch) with 1°×1° spatial
284 collocation were chosen in this evaluation. However, for some days, there was no noontime
285 granule in AIRS retrieval (nearly 35 out of total 242 soundings), then we used a loose collocation
286 of ±1 day. However, no significant changes were seen after such flexible collocation. Most of the
287 ozonesondes have burst altitudes near 10 hPa, hence AIRS ozone profiles are evaluated from
288 surface to 10 hPa.

289
290 Although suitable collocation criteria have been defined for a fair comparison, still different
291 vertical resolutions of the two data sets (ozonesonde ~100 m and AIRS ~1-5 km) make the
292 meaningful comparison difficult (Maddy and Barnett, 2008; Verstraeten et al., 2013; Boynard et
293 al., 2016). The difference in vertical resolution and retrieval sensitivity must be accounted for a
294 meaningful comparison. Though there is no perfect way to remove the error arising from the
295 different vertical resolutions of the two measurements, still utilizing the averaging kernel
296 smoothing or Gaussian smoothing, the error is minimized. Various groups have used the satellite
297 averaging kernels smoothing to compare satellite measurements with ozonesonde (Zhang et al.,
298 2010; Verstraeten et al., 2013; Boynard et al., 2016, 2018), while Gaussian smoothing (Wang et
299 al., 2020) and broad layer columns (Nalli et al., 2017) are also utilized. In the present analysis,
300 averaging kernel smoothing is utilized. First, ozonesonde data were interpolated at all AIRS
301 Radiative Transfer Algorithm (RTA) layers from surface to burst altitude, then ozonesonde
302 profiles were smoothed according to the AIRS averaging kernel and a-priori profile (ML
303 climatology), leading to a vertical profile [ozonesonde (AK)] representing what AIRS would have
304 measured for the same ozonesonde sampled atmospheric air mass in the absence of any other error
305 affecting satellite observations. According to Rodgers and Connor (2003), the smoothing of the
306 true state can be characterized as follows:

307
$$X_{\text{est}} = X_0 + A^{-1}(X_{\text{sonde}} - X_0) \quad (1)$$

308 The AIRS provides averaging kernels information at 9 pressure levels (Figure 2b) whereas the
309 AIRS RTA has 100 pressure levels. So following ozone vertices (Table S3) and formulating
310 trapezoid matrix (Figure 2a, the details regarding the calculation of trapezoid matrices are given

311 in AIRS/AMSU/HSB Version 6 Level 2 Product Levels, Layers and Trapezoids), we convert 9
312 levels AIRS averaging kernels to 100 levels averaging kernels using following defined operation.

$$313 \quad A' = F \times A_{\text{trapezoid}} \times F' \quad (2)$$

314 Where $A_{\text{trapezoid}}$ and F are averaging kernel matrices and trapezoid matrices (F' is pseudo-inverse
315 of F). $A_{\text{trapezoid}}$ is a given product, while F is calculated for given ozone vertices (Table S3).

316 Further, in the thermal IR spectrum, the contribution of ozone or any other trace gas towards
317 emission/absorption of IR radiation in the radiative transfer equation depends on the exponent of
318 layer integrated column amounts (Maddy and Barnett, 2008). Hence logarithmic changes in layer
319 column density are more linear than absolute changes. So logarithmic equations are used instead
320 of Eq. 1 for smoothing ozonesonde data in the present study.

$$321 \quad \ln(X_{\text{est}}) = \ln(X_0) + A' \{ \ln(X_{\text{sonde}}) - \ln(X_0) \} \quad (3)$$

322 Where X_{est} , X_{sonde} , and X_0 are smooth ozonesonde or ozonesonde (AK), true ozonesonde, and first
323 guess (ML climatology) profiles, respectively. [Knowing the nature of convolution from Eq. 1 and](#)
324 [3, it can be observed that the ozonesonde \(AK\) or smooth ozonesonde will have more weights](#)
325 [toward a-priori profiles when satellite retrieval is poor or AKs approaches zero values.](#)

326 More details on the calculation of averaging kernels can be found in AIRS documents
327 (AIRS/AMSU/HSB Version 6 Level 2 Product Levels, Layers and Trapezoids) or in available
328 literature (Maddy and Barnett, 2008; Irion et al., 2018). A typical averaging kernels matrix and
329 other parameters are shown in Figure 2. Figure 2a shows a typical trapezoid matrix, Figure 2b
330 shows the averaging kernels at 9 pressure levels, Figure 2c shows constructed averaging kernels
331 at 100 RTA layers, and Figure 2d shows an example of the different ozone profiles convolved with
332 AKs on 15 June 2011 over the observation site.

333

334 2.3 Statistical Analysis

335 The error analysis for AIRS retrieval with interpolated and smoothed ozonesonde is based on Nalli
336 et al. (2013, 2017). Bias, root mean squared error (RMSE), and standard deviation (STD) are
337 studied at various RTA vertical levels from the surface to 10hPa over the Himalayan region. The
338 finer spatio-temporal collocation utilized here has further minimized the uncertainty and error in
339 the evaluation. Since the observation site (29.4° N, 79.5° E) is at a latitude lower than 45°; hence
340 there is a lesser overlap of satellite passes, and mostly a few nadir scans are close to the observation
341 site (mostly daytime granules in the range of 75 to 85). Hence all the daytime observations of
342 AIRS are close to ± 3 hours of temporal collocation to the ozonesonde launch and possess a lesser
343 chance of time mismatch.

344

345 Given the collocated ozone mixing ratio profiles for satellite, ozonesonde (AK), and in-situ truth
346 (ozonesonde) observations, the statistical errors are calculated as follows -

347

$$348 \quad \text{RMSE } (\Delta O_l) = \sqrt{\frac{\sum_{j=1}^{j=n} W_{l,j} \times (\Delta O_{l,j})^2}{\sum_{j=1}^{j=n} W_{l,j}}} \quad (4)$$

349

$$350 \quad \text{Bias } (\Delta O_l) = \frac{\sum_{j=1}^{j=n} W_{l,j} \times (\Delta O_{l,j})}{\sum_{j=1}^{j=n} W_{l,j}} \quad (5)$$

351 Here l runs over different RTA layers and j runs for all collocated profiles, $\Delta O_{l,j}$ the fractional
352 deviation is taken to be the absolute deviation divided by the observed value. Where $\Delta O_{l,j} =$

353 $\left(\frac{O^R_{l,j} - O^T_{l,j}}{O^T_{l,j}}\right)$, O^T and O^R are ozonesonde/ozonesonde (AK) and satellite retrieved ozone mixing ratio,

354 respectively. $W_{1,j}$ is the weighting factor and assumes one of three forms $W_0 = 1$, $W_1 = O^R$ and W_2
 355 $= (O^R)^2$ and for ozone to minimize skewing impact due to large variation in mixing ratio at different
 356 altitudes, we have used the W_2 weight factor as suggested by other sounder science team (Nalli et
 357 al., 2013, 2017). The Standard deviation (STD) is then calculated by the square root of difference
 358 between RMSE and biases square at different RTA levels. Further to check the strength of the
 359 linear relationship between the satellites retrieved data and ozonesonde data the square of
 360 Pearson's correlation coefficient is also calculated.

361

362

363 **2.4 Estimation of Columnar Ozone**

364 The total column ozone (TCO) from ozonesonde is calculated by integrating the ozone mixing
 365 ratio from the surface to burst altitude and then adding residual ozone above burst altitude. Here
 366 the residual ozone is obtained from satellite-derived balloon-burst climatology (BBC) (McPeters
 367 [and Labow, 2012; Stauffer et al., 1997](#)2022). The discrete integration for calculation of total ozone
 368 column (DU) between defined boundaries is performed as follows:

$$369 \quad \text{Total column ozone} = 10^7 \times \left(\frac{RT_o}{g_o P_o} \right) \times \sum_{j=1}^{j=n} 0.5 \times (VMR[i] + VMR[i + 1]) \times (P[i] - P[i + 1]) \quad (6)$$

370

371 Where P is ambient pressure in hPa, VMR volume mixing ratio of ozone in ppbv, R (= 287.3 JKg⁻¹
 372 K⁻¹) gas constant, g_o (= 9.88 ms⁻²), P_o (= 1.01325×10⁵ Pa) and T_o (= 273.1 K) standard
 373 temperature.

374 The UTLS ozone column (DU) is also calculated using Eq. (6), where the UTLS region is defined
 375 between 400 hPa to 70 hPa (Bian et al., 2007). Additionally, the tropospheric ozone column (DU)
 376 is calculated for ozonesonde utilizing Eq. (6) with boundaries from the surface to the [lapse rate](#)

377 tropopause-[\(LRT\)](#). The tropopause height from balloon-borne observations is estimated using the
378 lapse rate method as well as the AIRS-derived tropopause is used and shown in Figure 3. However,
379 for OMI and MLS tropospheric ozone residual method is used, which calculates the tropospheric
380 ozone column by subtracting the OMI total column from MLS stratospheric ozone column
381 (Hudson et al., 1998; Ziemke et al., 2006).

382

383

384

385

386 **3. Results and Discussion**

387 **3.1 Ozone Distribution [Along](#) Balloon Trajectory: Ozonesonde and AIRS**

388 The distributions of ozone along the balloon tracks obtained using all ozone soundings data during
389 four seasons are shown in Figure 4. The nearest swath of AIRS ozone observations is interpolated
390 to the balloon locations and altitudes. Altitude variations of the balloon along longitude are
391 shown in Figure S3. The balloons drift to a very long-distance during winter, followed by autumn
392 and spring. During these seasons, balloons often reach Nepal also. The wind reversal took place
393 during the summer-monsoon when the balloon drifts towards IGP regions (Figure 4). The
394 distributions of ozone from AIRS are more-or-less similar to the distributions those from
395 ozonesonde. Here, the ozone variations are reflecting in terms of spatial as well as vertical
396 distributions. The bias and coefficient of determination (r^2) between ozonesonde and AIRS ozone
397 are studied along the longitude and latitude (Figures S3 and S4). Lower biases (lesser than 10%)
398 and higher r^2 are seen in the lower and middle troposphere. The poor correlation (<0.4) and larger
399 biases of up to 28% are seen at certain longitudes that are associated with higher altitudes (> 20

400 km). Around the balloon launch site (Nainital, 79.4545° E) highest r^2 score of 0.98 and low bias
401 of 1.4% are observed, which remain higher (r^2) and lower (bias) up to 80° E (Figure S3).

402
403

404

405 **3.2 Ozone Soundings and AIRS Ozone Profiles**

406 Figure 5 shows the average monthly ozone profiles for collocated observations of ozonesonde and
407 AIRS, respectively, during seven-year periods. The ozonesonde convolved with AIRS averaging
408 kernels [ozonesonde (AK)] and AIRS a-priori are also compared. The value of percentage
409 difference between ozonesonde (AK) and AIRS ozone at 706, 617, 496, 103, 29, and 14 hPa
410 altitudes are shown in figure 5, and the zoomed variations in the lower tropospheric ozone (surface
411 to 200 hPa) are also presented in the insets. AIRS slightly (~10%) underestimates ozone in the
412 lower troposphere during most of the months, except the summer-monsoon (June-August), where
413 an overestimation of up to 20% is observed. In the middle troposphere, around 300 hPa, an
414 underestimation in the range of 1 - 17% is seen for all months with an approaching tendency of
415 ozonesonde (AK) towards the true ozonesonde profiles. However, near the tropopause region,
416 AIRS retrievals considerably overestimate ozone by up to 102%. The overestimation was
417 highest for the winter season (82 - 102%), followed by the spring, and autumn, while lowest for
418 the summer-monsoon season (10 - 27%). In the stratosphere, where the sensitivity of AIRS is
419 higher (Figure 2c), the ozonesonde and AIRS differences were relatively lesser. Additionally,
420 AIRS retrieval shows an underestimation of 5 - 21% in this altitude region.

421

422 As expected, the difference between ozonesonde and AIRS is significantly reduced (Table 1) after
423 applying the averaging kernel or accounting for the sensitivity difference. This reduction was more
424 notable for the summer monsoon period near the tropopause, where the difference reduced from
425 92% to 19%, providing an improvement of 72%. The improvement ~~is~~was as high as 100% on a
426 monthly basis. Additionally, relative difference profiles were also analyzed for individual
427 soundings as well for the different seasons (Figure S5). Higher differences of about 150% between
428 AIRS and ozonesonde ozone observations were seen in the upper troposphere and lower
429 stratospheric (UTLS) region. The higher difference during winter and spring between these
430 observations in the UTLS region could be due to recurring ozone transport via tropopause folding
431 over the observation site. Such events may remain undetected by AIRS due to lower vertical
432 resolution leading to the missing of some tropopause folding events at lower altitudes (Figure 3).
433 However, in the lower troposphere, larger differences between ozonesonde and AIRS during
434 summer-monsoon are seen, which are due to low ozone and frequent cloudy conditions leading to
435 poor retrieval. The arrival of cleaner oceanic air during the south-west monsoon (or summer
436 monsoon) brings ozone-poor air and frequent cloudy conditions over northern India that weakens
437 the photochemical ozone production (Naja et al., 2014; Sarangi et al., 2014). Moreover, in the
438 lower troposphere, the limited sensitivity of hyperspectral satellite instruments has a significant
439 contribution from the a-priori information, which is also observed for AIRS retrieval (Figure 5).

440
441 Figure 6 shows the yearly time series analysis of the average ozone mixing ratio at four defined
442 layers, characterizing the middle troposphere (600 - 300 hPa), the upper troposphere (300 - 100
443 hPa), lower stratosphere (100 - 50 hPa), and middle stratosphere (50 - 10 hPa) respectively. A
444 prominent seasonality was seen in the time series throughout the years, which is quite clear in the

445 upper troposphere (300 - 100 hPa). The ozone seasonality contrast reflects the influence of
446 summer-monsoon and winter seasons. The seasonality contrast is similar between AIRS and
447 ozonesonde measurements, while a reversal of ozone seasonality is observed in the middle
448 stratospheric region compared to other layers. The opposite seasonality of the middle stratospheric
449 region is primarily due to dominant circulations, variation of solar radiation and dynamics. Total
450 column water vapor is also shown in Figure 6 that shows a tendency of anti-correlation with ozone
451 in the 300 - 100 hPa region.

452

453 We have also estimated the monsoon index by the difference between zonal (U) wind (MERRA-
454 [2_reanalysis_data](#)) at 850 hPa over the Arabian Sea (~~40~~40° E - ~~80~~ 80° E, ~~5~~ N - ~~15~~5° N - 15° N) and
455 over the central Indian landmass (~~70~~70° E - ~~90~~90° E, ~~20~~20° N - ~~30~~ 30° N) as done by Wang et al.
456 (2001).

457 In general, the positive values of the monsoon index correspond to strong monsoons and negative
458 values correspond to weak monsoon periods (Wang et al., 2001). During the weak monsoon, there
459 is relatively drier air, lower cloud cover and higher surface temperature compared to the strong
460 monsoon period (Lu et al., 2018). We observed a tendency of lower annual average ozone (from
461 ozonesonde and AIRS measurements) during greater (positive) monsoon index and higher annual
462 average ozone during lower (negative) monsoon index. Lu et al. (2018) have shown an anti-
463 correlation (0.46) of tropospheric ozone with monsoon index over the Indian region. The years
464 2011, 2012, 2014, and 2015 are classified as weak monsoon years and relatively higher ozone is
465 seen during these years, whereas for the years 2013, 2016, and 2017, strong monsoon is observed,
466 and average yearly ozone was lesser during these years (Figure 6 bottom left). The relative
467 difference of AIRS ozone with ozonesonde in the upper tropospheric region also shows an anti-

468 correlation (Figure 6) of 0.17 with total column water vapor. Furthermore, the larger ozone
469 differences between AIRS and ozonesonde are associated with the lower water vapor (Figure S6),
470 which may be arising due to the influence of ozone-sensitive water vapor (WV) channels in mid-
471 Infra-red regions. Further, in the middle troposphere (600-300 hPa), a secondary ozone peak in
472 post-monsoon is observed, which is suggested to be influenced by the biomass burning (Figure
473 S7) over northern India that seems to be missing in the AIRS ozone.

474
475 In the middle troposphere (600 - 300 hPa) and lower stratosphere (100 - 50 hPa), AIRS retrievals
476 show higher differences with respect to ozonesondes, while a nominal difference is observed for
477 the middle troposphere and middle stratosphere (Figure S6). Furthermore, a systematic increase in
478 standard deviation is also seen with the altitude. The higher standard deviations in the upper
479 tropospheric and stratospheric regions are mainly due to higher ozone variability associated with
480 stratosphere-troposphere exchange (STE) processes over the Himalayan region (Naja et al., 2016;
481 Bhardwaj et al., 2018).

482

483 **3.3 Statistical Analysis of AIRS Ozone Profiles**

484 Error analysis of AIRS retrieved ozone over the Himalayan region is performed with spatio-
485 temporal collocated ozonesonde observations as a reference. The methodology to calculate the
486 root mean square error (RMSE), bias, and standard deviation (STD) is described in section 2.3.
487 W_2 weighting statistics are utilized due to abrupt changes in atmospheric ozone with altitude. Here
488 bias and STD between AIRS and ozonesonde are calculated at different RTA layers from surface
489 to 10 hPa. Figure 7 shows the average variation of bias and STD at different RTA layers from
490 surface to 10 hPa over this region. The mean biases between ozonesonde and MLS, a high vertical

491 resolution satellite instrument, are also shown in figure 7. In general, higher positive biases (~65%)
492 and STDs (~25%) in AIRS ozone retrieval are seen in the UTLS region, where MLS agrees well
493 with ozonesonde. In the lower and middle troposphere, the AIRS ozone retrieval is negatively
494 biased (0 - 25%), which increases gradually from the surface to higher altitudes (~ [350hPa](#)
495 [hPa](#)). A negative bias was also seen in the stratosphere of about 15%. Similar to the biases, STDs
496 are also smaller in the lower troposphere and stratosphere, with values of nearly 15%. The higher
497 statistical errors in the upper troposphere and the lower stratospheric region could be due to lower
498 ozone partial pressure and frequent stratospheric to tropospheric transport events over the
499 Himalayas (Rawat et al., 2020, 2021), which introduces errors either after a mismatch of events in
500 AIRS coarser vertical resolution or due to complex topography. Additionally, the AIRS tropopause
501 frequency distribution shows less ability of AIRS to capture deep intrusion events (Figure 3).
502 Further, AIRS trace gas retrieval largely depends on successful temperature retrieval and uses
503 temperature retrieval as an input parameter (Maddy and Barnet, 2008). Hence, temperature
504 retrieval error could also propagate to ozone, and statistical error analysis of AIRS temperature
505 shows relatively higher biases (~ 2 K) in the upper tropospheric region (Figure S8).

506
507 The statistical error analysis was more-or-less similar for both true and smoothed ozonesonde
508 profiles. However, notable reduction in tropospheric bias and vertical shifts of errors were also
509 observed after applying the averaging kernel matrix to the true ozonesonde throughout the profile.
510 A shift of the error peak is seen from the lower stratosphere to the upper troposphere. This could
511 be due to the higher sensitivity of AIRS retrieval in the lower stratosphere, which would have
512 minimized the error at these particular altitudes. However, in the upper troposphere, higher

513 contribution of a-priories, as well as other factors (i.e., STE), might have resulted in larger biases
514 and errors.

515

516 The histogram of differences between AIRS and ozonesonde (AK) is also studied at [variousfour](#)
517 defined layers (Figure 8). AIRS mostly underestimated ozone with a mean bias of 2.37 ppbv, 9.29
518 ppbv, and 39.8 ppbv in 800 - 600 hPa, 600 - 300 hPa, and 100 - 50 hPa layers, respectively, while
519 in the upper troposphere (300 - 100 hPa) AIRS overestimated with a mean bias of 43.22 ppbv.
520 Furthermore, distributions of differences are skewed toward the negative values in the lower
521 stratosphere and towards positive values in the upper troposphere. A more symmetric distribution
522 over the negative axis is observed in the middle and lower troposphere. We also studied the
523 correlation profiles for different seasons (Figure 8, right panel). A strong correlation is seen in the
524 lower and middle troposphere for spring and summer, while there is a poor correlation for winter
525 and autumn. In the lower troposphere, a larger difference between AIRS and ozonesonde_(AK) is
526 observed, particularly during summer, with a relatively higher correlation mostly due to the greater
527 concurrence of AIRS a-priori with ozonesonde_(AK). Whereas, in the upper troposphere (300 -
528 100 hPa), a larger difference during winter and spring is primarily due to frequent subtropical
529 dynamics, while a higher correlation during the winter is mainly contributed from the AIRS
530 retrieval. Furthermore, analysis of the correlation coefficient between AIRS and ozonesonde over
531 different regions shows a higher correlation in the middle stratosphere (0.95) and lower
532 stratosphere (0.92), followed by upper troposphere (0.68), lower troposphere (0.62), and middle
533 troposphere (0.47).

534

535 **3.4 Assessment of AIRS Retrieval Algorithm with IASI and CrIS Radiance**

536 The MetOp/IASI and Soumi-NPP/CrIS radiance-based ozone products are assessed using
537 ozonesonde data over the central Himalayan region for one year (April 2014 to April 2015),
538 utilizing a total of 32 soundings. Here, the IASI and CrIS based ozone retrievals are research
539 products provided by NOAA, whose retrieval is based on the AIRS retrieval algorithm and follows
540 a similar averaging kernels matrix (Nalli et al., 2017). For IASI, due to the 09:30 ascending nodes
541 (morning overpass in India), ± 6 h loose temporal collocation is used. However, CrIS and AIRS
542 follow the same collocation due to a similar noontime overpass. The IASI, CrIS, and AIRS sensors
543 have 8461, 1305, and 2378 IR channels, respectively. Hence, analyzing their satellite ozone
544 products further helps to assess the AIRS retrieval algorithm for different IR radiances and channel
545 sets.

546
547 Figure 9a shows the seasonal ozone profiles obtained from three IR satellite sensors along with
548 ozonesonde for one year period. All sensors showed more-or-less similar ozone peak altitude and
549 ozone gradient. The estimated ozone peak altitude for ozonesonde, AIRS, IASI, and CrIS are 11.35
550 hPa, 10 hPa, 9.11 hPa, and 7.78 hPa, respectively. The estimated average ozone gradient in regions
551 between tropopause to gradient peak are 231.5 ppbv/hPa, 199.0 ppbv/hPa, 193.2 ppbv/hPa, and
552 199.1 ppbv/hPa for ozonesonde, AIRS, CrIS, and IASI, respectively.

553
554 Moreover, the higher ozone values during spring throughout the troposphere are captured well by
555 all satellite sensors. Higher ozone during spring and winter in the UTLS region is observed well
556 by AIRS and IASI, similar to ozonesonde but such features seem to be missing in CrIS ozone
557 retrieval. At the same time, CrIS sensitivity looks relatively low, where the possible role of the

558 number of channels can be seen. However, IASI and AIRS have effectively captured the ozone
559 seasonal variability.

560

561 Figure 9b shows the weighted statistical error analysis of IASI, CrIS, and AIRS ozone retrieval
562 with the true ozonesonde observations. Here, the difference in sensitivity of the two data sets is
563 not accounted for as this section's primary aim is to assess the AIRS retrieved algorithm using
564 different IR sensor radiances and channel sets. All three space-borne sensors overestimated UTLS
565 ozone by more than 50%, however, in the stratosphere and lower troposphere, the bias was slightly
566 lower, and it is somewhat underestimated. Similar to bias, the STDs were also higher in the UTLS
567 region by more than 60%. A consistent larger differences in the UTLS region for all three IR
568 satellite sensors that share the similar radiative transfer model and retrieval algorithm shows the
569 possible influence of complex topography and the various STE processes, in introducing errors in
570 retrieval processes, apart from input a-priories of the retrieval.

571

572 Additionally, Pearson correlations between ozonesonde and IASI, CrIS, and AIRS are also studied
573 at five atmospheric layers (i.e., 600-800 hPa, 300-600 hPa, 100-300 hPa, 50-100 hPa, and
574 10 - 50 hPa) (Table 2). A relatively stronger positive correlation is found in the middle stratosphere
575 (50-100 hPa) and lower stratosphere (50 - 100 hPa), which was highest for AIRS, followed by
576 CrIS and IASI, and a relatively low correlation is observed in the middle troposphere (300-600
577 hPa) for AIRS and IASI (~ 44% and 31%), while CrIS shows the poorest correlation in the lower
578 troposphere about 9%. The lower concurrence between ozonesonde and the satellite sensors in the
579 lower troposphere could be due to lower sensitivity and shorter lifetime of near-surface ozone that
580 could increase the a-priori contribution and sampling mismatch, respectively.

581

582 **3.5 Columnar Ozone**

583 **3.5.1 Total Column Ozone (TCO)**

584 Figure 10a shows variations in monthly average total column ozone (TCO) from ozonesonde,
585 AIRS, and OMI during 2011 - 2017. Here the box plots are also overlaid on the mean column to
586 describe the distribution of monthly column data. In general, the TCO is higher during spring,
587 which subsequently drops in summer-monsoon. AIRS TCO shows a bimodal monthly variation
588 which is not seen in the ozonesonde and OMI observations, otherwise, its monthly variation is in
589 reasonable agreement with ozonesonde. The OMI TCO is in a good match with the ozonesonde
590 with a maximum difference of up to about 5 DU. Table 3 shows the difference in the TCO between
591 AIRS, OMI, and ozonesonde. AIRS shows considerable overestimation in the range of 2.2 - 22
592 DU for some months while notable underestimation (1.8 - 4 DU) for others, with respect to both
593 ozonesonde and OMI. The correlation between AIRS TCO and ozonesonde TCO is found to be
594 0.5 (Table S4). To further understand the cause of bimodal variations in AIRS (higher ozone during
595 August, September, and October), the AIRS ozone profiles were integrated between different
596 stratospheric regions (100 - 70 hPa, 70 - 50 hPa, 50 - 20 hPa, and 20 - 1 hPa) and we found that
597 the elevated total ozone during post-monsoon is mainly contributed from the altitude above 50
598 hPa.

599

600 **3.5.2 UTLS Ozone Column**

601 Figure 10b shows the variations in the monthly average UTLS ozone column for collocated and
602 concurrent observations of AIRS, MLS, and ozonesonde during 2011 - 2017. The UTLS region
603 extends between 400 hPa to 70 hPa (Bian et al., 2007) for ozonesonde and AIRS, while for MLS,

604 the region between 261 hPa to 70 hPa is utilized. The recommended pressure levels for MLS v4
605 ozone retrieval are above 261 hPa (Livesey et al., 2013; Schwartz et al., 2015). In contrast to TCO,
606 higher ozone in UTLS is seen during the winter and spring (~ 45 DU) when there are recurring
607 downward transport events, while a clear drop of the column during the summer-monsoon shows
608 the convective transport of cleaner oceanic air to the higher altitudes. All the collocated
609 observations are able to capture the monthly variation effectively. However, there is a substantial
610 overestimation by more than 3 DU (Table S5) for all the months in AIRS measurements and MLS
611 mostly underestimate it, except during winter due to smaller integrated columns. Furthermore, the
612 larger whiskers of the box plot during winter and spring show the larger variations of the ozone in
613 the UTLS region. Though there were notable overestimations compared to ozonesonde, still UTLS
614 monthly variations are captured well by AIRS with a correlation of up to 75% (Table S4). In
615 addition, the correlation of ozonesonde and AIRS ozone at each pressure level in the UTLS region
616 is 0.81, which further increases with ozonesonde_AK (of about 0.94). The persistent biases in the
617 satellite retrievals arises due to inadequate input parameters that can be improved by using more
618 accurate initial parameters and surface emissivity (Dufour et al., 2012; Boynard et al., 2018).

619

620

621 **3.5.3 Tropospheric Ozone Column**

622 Figure 10c shows the variations in the monthly average tropospheric ozone column utilizing
623 various collocated data sets during 2011 - 2017. The tropospheric ozone column is calculated by
624 integrating ozone profiles from the surface to the tropopause. WMO-defined lapse rate calculation
625 method is used to calculate tropopause height from balloon-borne and AIRS observations (Figure
626 3). Higher tropospheric ozone is observed during the spring and early summer (> 45 DU) when

627 annual crop-residue burning (Figure S7) events occur over northern India, apart from downward
628 transport from the stratosphere. A few cases of downward transport are discussed in the next
629 section. The tropospheric ozone column drops rapidly during the summer-monsoon when pristine
630 marine air reaches Nainital. A slight increase of column is also seen during the autumn, which is
631 again influenced by post-monsoon crop residue burning practices (Figure S7) over northern India
632 (Bhardwaj et al., 2016). The AIRS is able to capture the monthly variations very effectively;
633 however, there are larger biases. The biases with ozonesonde are higher when the tropopause is
634 taken from the balloon-borne observation, while with AIRS provided tropopause, the biases are
635 lesser or mostly within the one sigma limit. The correlation between ozonesonde and AIRS, when
636 used AIRS tropopause, is very strong (0.72). Like AIRS, the OMI/MLS column is in good
637 agreement and able to produce monthly variations; however, there are larger differences during
638 winter and spring of more than 10 DU. The tropospheric ozone column from ozonesonde is
639 different for balloon-borne LRT and AIRS tropopause, which could be due to the lower vertical
640 resolution of AIRS. AIRS calculates tropopause with an uncertainty of 1-2 km (Divakarla et al.,
641 2006). It can also be seen that on average a lower (about 28%) tropopause pressure (or higher
642 altitude) is calculated by AIRS compare to ozonesonde measurements (Figure 3).

643

644 **3.6 Case Studies of Biomass Burning and Downward Transport** ---

645 Over northern India, extensive agriculture practices and forest fires influence ozone at the surface
646 and higher altitudes (Kumar et al., 2011; Cristofanelli et al., 2014; Bhardwaj et al., 2016; Bhardwaj
647 et al., 2018). Based on MODIS fire counts, the days in between 1 March to 15 April over northern
648 India are classified as the low fire periods (LFP) as considered in previous studies over this region.
649 The high fire period (HFP) is classified when the fire counts over the observational site are more

650 than the median fire counts in the biomass burning period, typically from mid-April to May
651 (Bhardwaj et al., 2016). A total of 32 soundings (mid-April to May) are classified as HFP and 33
652 soundings (March to mid-April) are classified as LFP. Figure 11 (left) shows the average ozone
653 profiles up to 6 km from ozonesonde and AIRS observations during HFP and LFP. The
654 ozonesonde data show enhancement in ozone by about 5 ppbv to about 11 ppbv during HFP as
655 compared to LFP that is accounting for a 5-20% increase. It is important to mention that
656 enhancement is greater in higher altitude regions that drop gradually above 400 hPa. The
657 enhancement is slightly lower (10-15%) in the AIRS profile, where most of it is contributed by
658 the a-priori profile (Figure S8).

659
660 Deep stratospheric intrusion or the downward transport (DT) of ozone-rich air from the
661 stratosphere to the troposphere significantly influences ozone profiles over the subtropical regions
662 (Collins, et al., 2003; Zhu, et al., 2006; Lal et al., 2014). Over the subtropical Himalayas, such
663 ozone intrusions are observed during the winter and spring seasons (Zhu et al., 2006; Ojha et al.,
664 2014). The DT events are classified based on the higher ozone in middle - upper troposphere seen
665 from ozonesonde with relatively larger Ertel potential vorticity (EPV) and lower humidity in
666 MERRA-2 reanalysis data. Based on this, 10 soundings (between January and mid-April) are
667 classified as DT events for ozonesonde and AIRS. Figure 11 (right) shows ozone profiles from
668 ozonesonde (AK) and AIRS observations for high ozone DT events as well as the average ozone
669 profiles of corresponding months excluding the DT event. Though there are persistent positive
670 biases in AIRS ozone profile compared to ozonesonde in the middle/upper troposphere, still both
671 the observations have captured the influence of the downward transport on the ozone profile very
672 effectively and show an increase in the ozone of 10 - 20% in altitude range 2 - 16 km. Ozonesonde

673 based observations have shown about twofold increase in upper-middle tropospheric ozone due to
674 downward ozone transport over this region (Ojha et al., 2014). Further, the first guess profile's
675 contribution to AIRS retrieval during DTs is negligible (Figure S9) and shows the main
676 contribution from the AIRS observations itself. So, despite the persistent biases in the AIRS and
677 ozonesonde observations, AIRS is able to capture the influences of downward transport (DT) on
678 ozone profile notably well.

679

680

681

682

683 **3.7 Ozone Radiative Forcing**

684 Radiative forcing is a valuable metric to estimate the radiative impacts of any anthropogenic or
685 natural activity on the climate system (Ramaswamy et al., 2001). It measures the net radiation at
686 the surface, tropopause, and the top of the atmosphere due to any atmospheric constituents. Here
687 we discuss the ozone radiative forcing (RF) at the surface in the ultraviolet (UV) spectral range
688 (Antón et al., 2014; Mateos et al., 2020) using the ozonesonde, OMI, and AIRS total column ozone
689 (TCO) data. The RF is calculated based on Antón et al. (2014), relative to 1979 utilizing TOMS
690 TOC data in 1979, monthly averaged solar zenith angles of site, clearness index based on
691 Chakraborty et al., (2014) and Hawas et al., (1984), and respective monthly average TCO data of
692 AIRS, OMI, and ozonesonde. Rather than quantifying the RF values here, our primary focus is to
693 show how the discrepancies of satellite ozone data (mainly AIRS) can impact the calculation of
694 RF values. Figure 12 shows the seasonal average ozone radiative forcing (RF) relative to 1979.

695 The annual average ozone RF during 2011 - 2017 is 4.86, 4.04, and 2.96 $\text{mW/m}^2\text{mWm}^{-2}$ for

696 ozonesonde, OMI, and AIRS, respectively. The RF values for ozonesonde and OMI are
697 comparable to Mateos et al. (2020) ($4 \text{ mW/m}^2 \text{ mWm}^{-2}$) for the extratropical region. However, for
698 AIRS, the RF value is lower by 45%. Further, the seasonal average ozone RF (2011-2017) is
699 consistent between ozonesonde and OMI, while notable differences are seen in AIRS except
700 during the winter season when differences are marginal (Figure 12). Also ~~from Table 3~~, it is
701 ~~clear~~noted (Table 3) that the higher total ozone bias during autumn (as high as 22 DU) contributes
702 to higher RF differences in autumn (Figure 12).

703

704 4. Summary and Conclusions

705 This study has utilized 242 ECC (EN-SCI) ozone soundings (during 2011 - 2017) conducted over
706 the Himalayan station (Nainital) to evaluate the AIRS version 6 ozone product and study the
707 performance during biomass burning events, ozone downward transport events and estimation of
708 ozone radiative forcing. AIRS ozone retrieval is evaluated in terms of retrieval sensitivity, retrieval
709 biases, retrieval errors, and ability to retrieve the natural variability of columnar ozone at different
710 altitude regions. This study is the first of its kind in the Himalayan region. The AIRS averaging
711 kernels information was applied to ozonesonde for a like-for-like comparison to overcome their
712 sensitivity differences. The monthly profile evaluation shows ozone peak and ozone altitude
713 dependency is captured well by AIRS retrieval with smaller but notable underestimation (5 - 20%)
714 in the lower-middle troposphere and stratosphere, while overestimation in the UTLS region as high
715 as 102%. We show ~~the larger~~a relatively higher sensitivity of AIRS ozone for the summer monsoon
716 in the UTLS region, where the biases between AIRS and ozonesonde ~~improved-remarkably~~reduced
717 ~~from 92% to 19 %~~ after applying AIRS averaging kernel information.

718

Formatted: Font color: Black

Formatted: Normal (Web), Space Before: 12 pt

Formatted: Font color: Black

719 ~~The~~Furthermore, the weighted statistical error analysis of AIRS retrieved ozone profiles [with](#)
720 [ozonesonde](#) shows higher positive biases (65%) and STD (25%) in the upper troposphere. ~~In~~While
721 [in](#) the lower ~~and~~ middle troposphere [and stratosphere](#), AIRS ozone was negatively biased, ~~apart~~
722 ~~from the stratosphere. of less than 20%.~~ In addition, though the biases and errors are higher in the
723 upper troposphere, there is a larger correlation of about 81% ~~showing%, demonstrating~~ the
724 [reasonable](#) capability of AIRS to retrieve upper tropospheric ozone variability with certain positive
725 biases ~~that~~. [Such biases in satellite retrieval](#) can be eliminated by choosing better emissivity inputs
726 or other retrieval [inputs parameters](#).

727
728 [The histogram of differences between AIRS and ozonesonde \(AK\) demonstrated that AIRS mostly](#)
729 [underestimated ozone \(2.37 - 39.8 ppbv\), while a notable overestimation with a mean bias of about](#)
730 [43 ppbv is seen in the upper troposphere.](#) The AIRS ozone retrieval algorithm was further
731 evaluated using the radiance of IASI and CrIS sensors; these sensors provided similar error
732 statistics as seen for AIRS, [with higher positive biases in the UTLS region](#).

733
734 The AIRS-derived columnar ozone amounts (i.e., total, UTLS, and tropospheric ozone) are also
735 evaluated to see whether the ozone variability at different altitude regions is being retrieved
736 correctly. The UTLS and tropospheric ozone monthly variations are captured well by AIRS with
737 persistent positive biases. However, the total ozone column shows bimodal monthly variations,
738 which was not evident in the ozonesonde and OMI total ozone observations. Further, we found a
739 higher total ozone column in AIRS during autumn, which is mostly coming from the stratospheric
740 region above 50 hPa. ~~The~~Furthermore, the capabilities of AIRS [ozone retrieval](#) to capture various
741 biomass burning and downward transport events have also been studied ~~using fire counts and~~

742 [EPV tracers](#). AIRS captures ~~at~~[reasonable enhancements in ozone profiles \(5 - 20%\) after](#) such
743 events ~~reasonably well~~ with notable contributions of the a-priori, particularly in ~~the biomass-~~
744 burning events.

745
746 Unlike the well-mixed greenhouse gases, the ozone radiative forcing (RF) remains uncertain due
747 to inadequate budget estimates and complex chemical processes. ~~The total ozone discrepancies of~~
748 ~~AIRS lead to show lower RF (by about 45%) and greater uncertainty in this Himalayan region.~~
749 Stevenson et al. (2013) have shown that a few percent uncertainties in ozone concentrations can
750 produce a spread of ~17% in ozone RF estimations. [The total ozone discrepancies of AIRS lead to](#)
751 [show lower RF \(by about 45%\) compared to ozonesonde and OMI and higher uncertainty in this](#)
752 [Himalayan region](#). Here, the role of in-situ observations from ozone soundings is shown to be
753 important in improving the satellite-~~retrieved~~ ozone over the Himalayan region by assessing and
754 providing insights upon its ~~err~~[errors](#) and ~~bia~~[biases](#). This information could be applied to the
755 ozone retrieval from other satellite data sets, ~~h~~ having long-term coverage. This will help ~~in~~ better
756 ~~understanding~~[understand](#) regional ozone and radiation budgets over this Himalayan region ~~having~~
757 ~~complex topography, and offer an opportunity to understand possible differences between~~
758 [satellites and truth observations](#).

759 **Acknowledgments**

760
761 We are grateful to Director ARIES and ISRO-ATCTM project for supporting this work. Help from
762 Deepak and Nitin in balloon launches and coordination with the air traffic control is highly
763 acknowledged. The National Center for Atmospheric Research is sponsored by the National
764 Science Foundation. SL is grateful to INSA, New Delhi for the position and Director PRL,

765 Ahmedabad for the support. We highly acknowledge NOAA and NASA-EARTHDATA online
766 data portals for providing IASI, AIRS, and CrIS level2 data. We thank the NASA Goddard Space
767 Flight Center Ozone Processing Team for providing the OMI/MLS tropospheric ozone, OMI total
768 ozone column and JPL for MLS ozone profile. We would also like to acknowledge the use of the
769 MODIS fire data through FIRMS archive download. Use of map from Google earth is also
770 acknowledged. We thank the reviewers for their constructive comments and valuable suggestions.

771

772

773 **Data availability:** Satellite data are available in the respective web portal. Ozone sonde data could
774 be made available on a reasonable request by writing to the corresponding author.

775

776 **References**

777 Antón, M., D. Mateos, R. Román, A. Valenzuela, L. Alados-Arboledas, and F. J. Olmo.: A method
778 to determine the ozone radiative forcing in the ultra-violet range from experimental data, *J.*
779 *Geophys. Res. Atmos.*, 119, 1860–1873, doi:10.1002/2013JD020444, 2014.

780

781 Aghedo, A.M., Bowman, K.W., Worden, H.M., Kulawik, S.S., Shindell, D.T., Lamarque, J.F.,
782 Faluvegi, G., Parrington, M., Jones, D.B.A. and Rast, S.: The vertical distribution of ozone
783 instantaneous radiative forcing from satellite and chemistry climate models. *Journal of*
784 *Geophysical Research: Atmospheres*, 116(D1), 2011.

785

786 Bai, W., Wu, C., Li, J. and Wang, W.: Impact of terrain altitude and cloud height on ozone remote
787 sensing from satellite, *Journal of Atmospheric and Oceanic Technology*, 31(4), pp.903-912, 2014.

788

789 Barre, J., Peuch, V.H., Attié, J.L., Amraoui, L.E., Lahoz, W.A., Josse, B., Claeysman, M. and
790 Nedelec, P.: Stratosphere-troposphere ozone exchange from high resolution MLS ozone analyses,
791 *Atmos. Chem. Phys.*, 12(14), pp.6129-6144, 2012.

792

793 Bhardwaj, P., Naja, M., Kumar, R. and Chandola, H.C.: Seasonal, interannual, and long-term
794 variabilities in biomass burning activity over South Asia, *Environmental Science and Pollution*
795 *Research*, 23(5), pp.4397-4410, 2016.

796

797 Bhardwaj, P., Naja, M., Rupakheti, M., Lupascu, A., Mues, A., Panday, A. K., Kumar, R., Mahata,
798 K. S., Lal, S., Chandola, H. C., and Lawrence, M. G.: Variations in surface ozone and carbon
799 monoxide in the Kathmandu Valley and surrounding broader regions during SusKat-ABC field
800 campaign: role of local and regional sources, *Atmos. Chem. Phys.*, 18, 11949–11971,
801 <https://doi.org/10.5194/acp-18-11949-2018>, 2018.

802

803 Bhartia, P.K., McPeters, R.D., Mateer, C.L., Flynn, L.E. and Wellemeyer, C.: Algorithm for the
804 estimation of vertical ozone profiles from the backscattered ultraviolet technique, *J. Geophys. Res.*
805 *Atmos.*, 101(D13), pp.18793-18806, 1996.

806

807 Bian, J., Gettelman, A., Chen, H. and Pan, L.L.: Validation of satellite ozone profile retrievals
808 using Beijing ozonesonde data, *J. Geophys. Res. Atmos.*, 112(D6), 2007.

809

810 Boynard, A., Hurtmans, D., Koukouli, M.E., Goutail, F., Bureau, J., Safieddine, S., Lerot, C.,
811 Hadji-Lazaro, J., Wespes, C., Pommereau, J.P. and Pazmino, A.: Seven years of IASI ozone

812 retrievals from FORLI: validation with independent total column and vertical profile
813 measurements, *Atmos. Meas. Tech.*, 9(9), pp.4327-4353, 2016.

814

815 Boynard, A., Hurtmans, D., Garane, K., Goutail, F., Hadji-Lazaro, J., Koukouli, M. E., Wespes,
816 C., Vigouroux, C., Keppens, A., Pommereau, J.-P., Pazmino, A., Balis, D., Loyola, D., Valks, P.,
817 Sussmann, R., Smale, D., Coheur, P.-F., and Clerbaux, C.: Validation of the IASI
818 FORLI/EUMETSAT ozone products using satellite (GOME-2), ground-based (Brewer–Dobson,
819 SAOZ, FTIR) and ozonesonde measurements, *Atmos. Meas. Tech.*, 11, 5125–5152,
820 <https://doi.org/10.5194/amt-11-5125-2018>, 2018.

821

822 [Brunamonti S. et al.: Balloon-borne measurements of temperature, water vapor, ozone and aerosol](#)
823 [backscatter on the southern slopes of the Himalayas during StratoClim 2016–2017, *Atmos. Chem. Phys.*,](#)
824 [18, 15937–15957, <https://doi.org/10.5194/acp-18-15937-2018>, 2018.](#)

825

826 Chakraborty, S., Sadhu, P.K. and Nitai, P.A.L.: New location selection criterions for solar PV
827 power plant. *International Journal of Renewable Energy Research*, 4(4), pp.1020-1030, 2014.

828

829 Clerbaux, C., Hadji-Lazaro, J., Turquety, S., George, M., Coheur, P.F., Hurtmans, D., Wespes, C.,
830 Herbin, H., Blumstein, D., Tourniers, B. and Phulpin, T.: The IASI/MetOp1 Mission: First
831 observations and highlights of its potential contribution to GMES2, *Space Research Today*, 168,
832 pp.19-24, 2007.

833

834 Coheur, P.F., Barret, B., Turquety, S., Hurtmans, D., Hadji-Lazaro, J. and Clerbaux, C.: Retrieval
835 and characterization of ozone vertical profiles from a thermal infrared nadir sounder, *J. Geophys.*
836 *Res. Atmos.*, 110(D24), 2005.

837
838 Collins, W. J., R. G. Derwent, B. Garnier, C. E. Johnson, M. G. Sanderson, and D. S. Stevenson.:
839 Effect of stratosphere-troposphere exchange on the future tropospheric ozone trend, *J. Geophys.*
840 *Res.*, 108(D12), 8528, doi:10.1029/2002JD002617, 2003.

841
842 Cristofanelli, P., Putero, D., Adhikary, B., Landi, T.C., Marinoni, A., Duchi, R., Calzolari, F., Laj,
843 P., Stocchi, P., Verza, G. and Vuillermoz, E.: Transport of short-lived climate forcers/pollutants
844 (SLCF/P) to the Himalayas during the South Asian summer monsoon onset, *Environmental*
845 *Research Letters*, 9(8), p.084005, 2014.

846
847 Divakarla, M., Barnet, C., Goldberg, M., Maddy, E., Wolf, W., Flynn, L., Xiong, X., Wei, J., Zhou,
848 L. and Liu, X.: Validation of Atmospheric Infrared Sounder (AIRS) temperature, water vapor, and
849 ozone retrievals with matched radiosonde and ozonesonde measurements and forecasts, In
850 *Multispectral, Hyperspectral, and Ultraspectral Remote Sensing Technology, Techniques, and*
851 *Applications*, International Society for Optics and Photonics, Vol. 6405, p. 640503, 2006.

852
853 Divakarla, M., Barnet, C., Goldberg, M., Maddy, E., Irion, F., Newchurch, M., Liu, X., Wolf, W.,
854 Flynn, L., Labow, G. and Xiong, X.: Evaluation of Atmospheric Infrared Sounder ozone profiles
855 and total ozone retrievals with matched ozonesonde measurements, ECMWF ozone data, and
856 Ozone Monitoring Instrument retrievals, *J. Geophys. Res. Atmos.*, 113(D15), 2008.

857

858 Dufour, G., Eremenko, M., Griesfeller, A., Barret, B., LeFlochmoën, E., Clerbaux, C., Hadji-
859 Lazaro, J., Coheur, P.F. and Hurtmans, D.: Validation of three different scientific ozone products
860 retrieved from IASI spectra using ozonesondes, *Atmos. Meas. Tech.*, 5(3), pp.611-630, 2012.

861

862 Ebi, K.L. and McGregor, G., Climate change, tropospheric ozone and particulate matter, and health
863 impacts, *Environmental health perspectives*, 116(11), pp.1449-1455, 2008.

864

865 Fadnavis, S., Dhomse, S., Ghude, S., Iyer, U., Buchunde, P., Sonbawne, S. and Raj, P.E.: Ozone
866 trends in the vertical structure of Upper Troposphere and Lower stratosphere over the Indian
867 monsoon region, *International Journal of Environmental Science and Technology*, 11(2), pp.529-
868 542, 2014.

869

870 Finlayson-Pitts, B.J. and Pitts, J.N.: Tropospheric air pollution: ozone, airborne toxics, polycyclic
871 aromatic hydrocarbons, and particles, *Science*, 276(5315), pp.1045-1051, 1997.

872

873 Fishbein, E., Farmer, C.B., Granger, S.L., Gregorich, D.T., Gunson, M.R., Hannon, S.E.,
874 Hofstadter, M.D., Lee, S.Y., Leroy, S.S. and Strow, L.L.: Formulation and validation of simulated
875 data for the Atmospheric Infrared Sounder (AIRS), *IEEE Transactions on Geoscience and Remote
876 Sensing*, 41(2), pp.314-329, 2003.

877

878 Fishman, J., Ramanathan, V., Crutzen, P.J. and Liu, S.C.: Tropospheric ozone and climate, *Nature*,
879 282(5741), pp.818-820, 1979.

880

881 Fishman, J., Minnis, P. and Reichle Jr, H.G.: Use of satellite data to study tropospheric ozone in
882 the tropics, *J. Geophys. Res. Atmos.*, 91(D13), pp.14451-14465, 1986.

883

884 Fishman, J. and Larsen, J.C.: Distribution of total ozone and stratospheric ozone in the tropics:
885 Implications for the distribution of tropospheric ozone, *J. Geophys. Res. Atmos.*, 92(D6), pp.6627-
886 6634, 1987.

887

888 Foret, G., Eremenko, M., Cuesta, J., Sellitto, P., Barré, J., Gaubert, B., Coman, A., Dufour, G.,
889 Liu, X., Joly, M. and Doche, C.: Ozone pollution: What can we see from space? A case study, *J.*
890 *Geophys. Res. Atmos.*, 119(13), pp.8476-8499, 2014.

891

892 Forster, P.M., Bodeker, G., Schofield, R., Solomon, S. and Thompson, D.: Effects of ozone cooling
893 in the tropical lower stratosphere and upper troposphere, *Geophysical Research Letters*, 34(23),
894 2007.

895

896 Fry, M.M., Naik, V., West, J.J., Schwarzkopf, M.D., Fiore, A.M., Collins, W.J., Dentener, F.J.,
897 Shindell, D.T., Atherton, C., Bergmann, D. and Duncan, B.N.: The influence of ozone precursor
898 emissions from four world regions on tropospheric composition and radiative climate forcing.
899 *Journal of Geophysical Research: Atmospheres*, 117(D7), 2012.

900

901 Gauss, M., Myhre, G., Pitari, G., Prather, M.J., Isaksen, I.S.A., Berntsen, T.K., Brasseur, G.P.,
902 Dentener, F.J., Derwent, R.G., Hauglustaine, D.A. and Horowitz, L.W.: Radiative forcing in the

903 21st century due to ozone changes in the troposphere and the lower stratosphere, *J. Geophys. Res.*
904 *Atmos.*, 108(D9), 2003.

905

906 Hauglustaine, D.A. and Brasseur, G.P.: Evolution of tropospheric ozone under anthropogenic
907 activities and associated radiative forcing of climate, *J. Geophys. Res. Atmos.*, 106(D23),
908 pp.32337-32360, 2001.

909

910 Hawas, M.M. and Muneer, T.; Study of diffuse and global radiation characteristics in
911 India. *Energy Conversion and Management*, 24(2), pp.143-149, 1984.

912

913 Hudson, R.D. and Thompson, A.M.: Tropical tropospheric ozone from total ozone mapping
914 spectrometer by a modified residual method, *J. Geophys. Res. Atmos.*, 103(D17), pp.22129-
915 22145, 1998.

916

917 Hegglin, M. I., Fahey, D. W., McFarland, M., Montzka, S. A., and Nash, E. R.: Twenty questions
918 and answers about the ozone layer: 2014 update, *Scientific Assessment of Ozone Depletion: 2014*,
919 84 pp., World Meteorological Organization, Geneva, Switzerland, ISBN 978-9966-076-02-1,
920 2015.

921

922 Irion, F.W., Kahn, B.H., Schreier, M.M., Fetzer, E.J., Fishbein, E., Fu, D., Kalmus, P., Wilson,
923 R.C., Wong, S. and Yue, Q.: Single-footprint retrievals of temperature, water vapor and cloud
924 properties from AIRS. *Atmospheric Measurement Techniques*, 11(2), pp.971-995, 2018.

925

926 Kim, J.H. and Newchurch, M.J.: Climatology and trends of tropospheric ozone over the eastern
927 Pacific Ocean: The influences of biomass burning and tropospheric dynamics, *Geophysical*
928 *research letters*, 23(25), pp.3723-3726, 1996.

929

930 Komhyr, W.D., Barnes, R.A., Brothers, G.B., Lathrop, J.A. and Opperman, D.P.: Electrochemical
931 concentration cell ozonesonde performance evaluation during STOIC 1989, *J. Geophys. Res.*
932 *Atmos.*, 100(D5), pp.9231-9244, 1995.

933

934 Komhyr, W.D.: Nonreactive gas sampling pump. *Review of Scientific Instruments*, 38(7), pp.981-
935 983, 1967.

936

937 Kumar, R., Naja, M., Satheesh, S.K., Ojha, N., Joshi, H., Sarangi, T., Pant, P., Dumka, U.C.,
938 Hegde, P. and Venkataramani, S.: Influences of the springtime northern Indian biomass burning
939 over the central Himalayas. *Journal of Geophysical Research: Atmospheres*, 116(D19), 2011.

940

941 Kumar, R., Naja, M., Pfister, G.G., Barth, M.C. and Brasseur, G.P.: Simulations over South Asia
942 using the Weather Research and Forecasting model with Chemistry (WRF-Chem): set-up and
943 meteorological evaluation, *Geoscientific Model Development*, 5(2), pp.321-343, 2012a.

944

945 Kumar, R., Naja, M., Pfister, G.G., Barth, M.C., Wiedinmyer, C. and Brasseur, G.P.: Simulations
946 over South Asia using the Weather Research and Forecasting model with Chemistry (WRF-
947 Chem): chemistry evaluation and initial results, *Geoscientific Model Development*, 5(3), pp.619-
948 648, 2012b.

949

950 Lacis, A.A., Wuebbles, D.J. and Logan, J.A.: Radiative forcing of climate by changes in the
951 vertical distribution of ozone, *J. Geophys. Res. Atmos.*, 95(D7), pp.9971-9981, 1990.

952

953 Lal S., S. Venkataramani, S. Srivastava, S. Gupta, M. Naja, T. Sarangi, X. Liu.: Transport effects
954 on the vertical distribution of tropospheric ozone over the tropical marine regions surrounding
955 India, *J. Geophys. Res.*, 118, 1513-1524, doi:10.1002/jgrd.50180, 2013.

956

957 Lal S., S. Venkataramani, N. Chandra, O. R. Cooper, J. Brioude, and M. Naja, Transport effects
958 on the vertical distribution of tropospheric ozone over western India, *J. Geophys. Res. Atmos.*,
959 119, doi:10.1002/2014JD021854, 2014.

960

961 Lal, S., Venkataramani, S., Naja, M., Kuniyal, J.C., Mandal, T.K., Bhuyan, P.K., Kumari, K.M.,
962 Tripathi, S.N., Sarkar, U., Das, T. and Swamy, Y.V.: Loss of crop yields in India due to surface
963 ozone: An estimation based on a network of observations, *Environmental Science and Pollution*
964 *Research*, 24(26), pp.20972-20981, 2017.

965

966 Lawrence, M.G. and Lelieveld, J.: Atmospheric pollutant outflow from southern Asia: a review,
967 *Atmospheric Chemistry and Physics*, 10(22), pp.11017-11096, 2010.

968

969 Lelieveld, J., Haines, A. and Pozzer, A.: Age-dependent health risk from ambient air pollution: a
970 modelling and data analysis of childhood mortality in middle-income and low-income countries,
971 *The lancet Planetary health*, 2(7), pp.e292-e300, 2018.

972
973 Livesey, N.J., Logan, J.A., Santee, M.L., Waters, J.W., Doherty, R.M., Read, W.G., Froidevaux,
974 L. and Jiang, J.H.; Interrelated variations of O₃, CO and deep convection in the
975 tropical/subtropical upper troposphere observed by the Aura Microwave Limb Sounder (MLS)
976 during 2004–2011. *Atmospheric Chemistry and Physics*, 13(2), pp.579-598, 2013.

977
978 Logan, J.A.: Tropospheric ozone: Seasonal behavior, trends, and anthropogenic influence, *J.*
979 *Geophys. Res. Atmos.*, 90(D6), pp.10463-10482, 1985.

980
981 Lu, X., Zhang, L., Liu, X., Gao, M., Zhao, Y. and Shao, J., 2018. Lower tropospheric ozone over
982 India and its linkage to the South Asian monsoon. *Atmospheric Chemistry and Physics*, 18(5),
983 pp.3101-3118.

984
985 Maddy, E.S. and Barnett, C.D.: Vertical resolution estimates in version 5 of AIRS operational
986 retrievals, *IEEE Transactions on Geoscience and Remote Sensing*, 46(8), pp.2375-2384, 2008.

987
988 Mateos, D. and Antón, M.: Worldwide Evaluation of Ozone Radiative Forcing in the UV-B Range
989 between 1979 and 2014. *Remote Sensing*, 12(3), p.436, 2020.

990
991 McPeters, R.D., Miles, T., Flynn, L.E., Wellemeyer, C.G. and Zawodny, J.M.: Comparison of
992 SBUV and SAGE II ozone profiles: Implications for ozone trends, *J. Geophys. Res. Atmos.*,
993 99(D10), pp.20513-20524, 1994.

994

995 ~~[McPeters, R.D., Labow, G.J. and Johnson, B.J.: A satellite derived ozone climatology for](#)~~
996 ~~[balloonsonde estimation of total column ozone, J. Geophys. Res. Atmos., 102\(D7\), pp.8875-8885,](#)~~
997 ~~[1997.](#)~~

998
999 McPeters, R.D., Labow, G.J. and Logan, J.A.: Ozone climatological profiles for satellite retrieval
1000 algorithms, J. Geophys. Res. Atmos., 112(D5), 2007.

1001
1002 [McPeters, R.D. and Labow, G.J.: Climatology 2011: An MLS and sonde derived ozone](#)
1003 [climatology for satellite retrieval algorithms. Journal of Geophysical Research:](#)
1004 [Atmospheres, 117\(D10\), 2012.](#)

1005 Monahan, K.P., Pan, L.L., McDonald, A.J., Bodeker, G.E., Wei, J., George, S.E., Barnet, C.D. and
1006 Maddy, E.: Validation of AIRS v4 ozone profiles in the UTLS using ozonesondes from Lauder,
1007 NZ and Boulder, USA, J. Geophys. Res. Atmos., 112(D17), 2007.

1008
1009 Monks, P.S., Archibald, A.T., Colette, A., Cooper, O., Coyle, M., Derwent, R., Fowler, D.,
1010 Granier, C., Law, K.S., Mills, G.E. and Stevenson, D.S.: Tropospheric ozone and its precursors
1011 from the urban to the global scale from air quality to short-lived climate forcer. Atmospheric
1012 Chemistry and Physics, 15(15), pp.8889-8973, 2015.

1013
1014 Munro, R., Siddans, R., Reburn, W.J. and Kerridge, B. J.: Direct measurement of tropospheric
1015 ozone distributions from space, Nature, 392(6672), pp.168-171, 1998.

1016
1017 Myhre, G., Aas, W., Cherian, R., Collins, W., Faluvegi, G., Flanner, M., Forster, P., Hodnebrog,
1018 Ø., Klimont, Z., Lund, M.T. and Mülmenstädt, J.: Multi-model simulations of aerosol and ozone

1019 radiative forcing due to anthropogenic emission changes during the period 1990–2015.
1020 Atmospheric Chemistry and Physics, 17(4), pp.2709-2720, 2017.
1021
1022 Naja, M., C Mallik, T. Sarangi, V Sheel, S. Lal, SO₂ measurements at a high altitude site in the
1023 central Himalayas: Role of regional transport, Atmospheric Environment,
1024 doi:10.1016/j.atmosenv.2014.08.031, 2014.
1025
1026 Naja M., Piyush Bhardwaj, N. Singh, Phani Kumar, R. Kumar, N. Ojha, Ram Sagar, S. K.
1027 Satheesh, K. Krishna Moorthy and V. R. Kotamarthi: High-frequency vertical profiling of
1028 meteorological parameters using AMF1 facility during RAWEX–GVAX at ARIES, Nainital,
1029 Current Science, vol 111, issue 1, 2016.
1030
1031 Nalli, N.R., Barnet, C.D., Reale, A., Tobin, D., Gambacorta, A., Maddy, E.S., Joseph, E., Sun, B.,
1032 Borg, L., Mollner, A.K. and Morris, V.R.: Validation of satellite sounder environmental data
1033 records: Application to the Cross-track Infrared Microwave Sounder Suite, J. Geophys. Res.
1034 Atmos., 118(24), pp.13-628, 2013.
1035
1036 Nalli, N.R., Gambacorta, A., Liu, Q., Tan, C., Iturbide-Sanchez, F., Barnet, C.D., Joseph, E.,
1037 Morris, V.R., Oyola, M. and Smith, J.W.: Validation of Atmospheric Profile Retrievals from the
1038 SNPP NOAA-Unique Combined Atmospheric Processing System. Part 2: Ozone, IEEE
1039 Transactions on Geoscience and Remote Sensing, 56(1), pp.598-607, 2017.
1040

1041 Nassar, R., Logan, J.A., Worden, H.M., Megretskaja, I.A., Bowman, K.W., Osterman, G.B.,
1042 Thompson, A.M., Tarasick, D.W., Austin, S., Claude, H. and Dubey, M.K. Validation of
1043 Tropospheric Emission Spectrometer (TES) nadir ozone profiles using ozonesonde measurements.
1044 Journal of Geophysical Research: Atmospheres, 113(D15), 2008.
1045
1046 Ojha, N., Naja, M., Sarangi, T., Kumar, R., Bhardwaj, P., Lal, S., Venkataramani, S., Sagar, R.,
1047 Kumar, A. and Chandola, H.C.: On the processes influencing the vertical distribution of ozone
1048 over the central Himalayas: Analysis of yearlong ozonesonde observations, Atmospheric
1049 Environment, 88, pp.201-211, 2014.
1050
1051 Pagano, T.S., Aumann, H.H., Hagan, D.E. and Overoye, K.: Pre-launch and in-flight radiometric
1052 calibration of the Atmospheric Infrared Sounder (AIRS), IEEE transactions on geoscience and
1053 remote sensing, 41(2), pp.265-273, 2003.
1054
1055 Pierce, R.B., Al-Saadi, J., Kittaka, C., Schaack, T., Lenzen, A., Bowman, K., Szykman, J., Soja,
1056 A., Ryerson, T., Thompson, A.M. and Bhartia, P.: Impacts of background ozone production on
1057 Houston and Dallas, Texas, air quality during the Second Texas Air Quality Study field mission,
1058 J. Geophys. Res. Atmos., 114(D7), 2009.
1059
1060 Pittman, J.V., Pan, L.L., Wei, J.C., Irion, F.W., Liu, X., Maddy, E.S., Barnet, C.D., Chance, K.
1061 and Gao, R.S.: Evaluation of AIRS, IASI, and OMI ozone profile retrievals in the extratropical
1062 tropopause region using in situ aircraft measurements, J. Geophys. Res. Atmos., 114(D24), 2009.
1063

1064 Ramaswamy, V., Boucher, O., Haigh, J., Hauglustaine, D., Haywood, J., Myhre, G., Nakajima,
1065 T., Shi, G.Y. and Solomon, S.: Radiative forcing of climate change. Climate change 2001: the
1066 scientific basis. Contribution of working group I to the third assessment report of the
1067 intergovernmental panel on climate change. DJ Griggs, M Noguer, PJ van der Linden, X Dai, K
1068 Maskell and CA Johnson (Cambridge: Cambridge University Press) pp, 350, p.416, 2001.
1069
1070 Rawat, P., Naja, M., Thapliyal, P.K., Srivastava, S., Bhardwaj, P., Kumar, R., Bhattacharjee, S.,
1071 Venkatramani, S., Tiwari, S.N. and Lal, S.: Assessment of vertical ozone profiles from INSAT-
1072 3D sounder over the Central Himalaya. Current Science, 119(7), p.1113, 2020.
1073
1074 Rawat, P. and Naja, M.: Remote sensing study of ozone, NO₂, and CO: some contrary effects of
1075 SARS-CoV-2 lockdown over India. Environ Sci Pollut Res, [https://doi.org/10.1007/s11356-021-](https://doi.org/10.1007/s11356-021-17441-2)
1076 17441-2, 2021.
1077
1078 Rodgers, C.D., 1976. Retrieval of atmospheric temperature and composition from remote
1079 measurements of thermal radiation. Reviews of Geophysics, 14(4), pp.609-624.
1080
1081 Rodgers, C.D., 1990. Characterization and error analysis of profiles retrieved from remote
1082 sounding measurements. Journal of Geophysical Research: Atmospheres, 95(D5), pp.5587-5595.
1083
1084 Rodgers, C.D. and Connor, B.J., 2003. Intercomparison of remote sounding instruments. Journal
1085 of Geophysical Research: Atmospheres, 108(D3).
1086

1087 Sarangi T., M. Naja, N. Ojha, R. Kumar, S. Lal, S. Venkataramani, A. Kumar, R. Sagar and H. C.
1088 Chandola: First simultaneous measurements of ozone, CO and NO_y at a high altitude regional
1089 representative site in the central Himalayas, J. Geophys. Res., 119, doi:10.1002/2013JD020631,
1090 2014.

1091
1092 Schwartz, M., Froidevaux, L., Livesey, N. and Read, W.: MLS/Aura Level 2 Ozone (O₃) Mixing
1093 Ratio V004, Greenbelt, MD, USA, Goddard Earth Sciences Data and Information Services Center
1094 (GES DISC), 10.5067/Aura/MLS/DATA2017, 2015.

1095
1096 Shindell, D., Kuylenstierna, J.C., Vignati, E., van Dingenen, R., Amann, M., Klimont, Z.,
1097 Anenberg, S.C., Muller, N., Janssens-Maenhout, G., Raes, F. and Schwartz, J.: Simultaneously
1098 mitigating near-term climate change and improving human health and food security, Science,
1099 335(6065), pp.183-189, 2012.

1100
1101 Smit, H.G., Straeter, W., Johnson, B.J., Oltmans, S.J., Davies, J., Tarasick, D.W., Hoegger, B.,
1102 Stubi, R., Schmidlin, F.J., Northam, T. and Thompson, A.M.: Assessment of the performance of
1103 ECC-ozonesondes under quasi-flight conditions in the environmental simulation chamber:
1104 Insights from the Juelich Ozone Sonde Intercomparison Experiment (JOSIE), Journal of
1105 Geophysical Research: Atmospheres, 112(D19), 2007.

1106 [Smit, H. G. J., Thompson, A. M., & ASOPOS Panel. \(2020\). ASOPOS 2.0: Assessment of](#)
1107 [Standard Operating Procedures for Ozone Sondes, WMO/GAW Report.](#)

1108

1109 Srivastava S., Manish Naja, V. Thouret: Influences of regional pollution and long range transport
1110 over Hyderabad using ozone data from MOZAIC, Atmospheric Environment, 117, pp.135-146,
1111 2015.

1112
1113 [Stauffer, R.M., Thompson, A.M., Kollonige, D.E., Tarasick, D.W., Van Malderen, R., Smit, H.G.,
1114 Vömel, H., Morris, G.A., Johnson, B.J., Cullis, P.D. and Stübi, R.: An examination of the recent
1115 stability of ozonesonde global network data. Earth and Space Science, 9\(10\), p.e2022EA002459,
1116 2022.](#)

1117
1118 Stevenson, D.S., Young, P.J., Naik, V., Lamarque, J.F., Shindell, D.T., Voulgarakis, A., Skeie,
1119 R.B., Dalsoren, S.B., Myhre, G., Berntsen, T.K. and Folberth, G.A.: Tropospheric ozone changes,
1120 radiative forcing and attribution to emissions in the Atmospheric Chemistry and Climate Model
1121 Intercomparison Project (ACCMIP), Atmos. Chem. Phys., 13(6), pp.3063-3085, 2013.

1122
1123 Susskind, J., Barnet, C.D. and Blaisdell, J.M.: Retrieval of atmospheric and surface parameters
1124 from AIRS/AMSU/HSB data in the presence of clouds, IEEE Transactions on Geoscience and
1125 Remote Sensing, 41(2), pp.390-409, 2003.

1126
1127 Susskind, J., Barnet, C., Blaisdell, J., Iredell, L., Keita, F., Kouvaris, L., Molnar, G. and Chahine,
1128 M.: Accuracy of geophysical parameters derived from Atmospheric Infrared Sounder/Advanced
1129 Microwave Sounding Unit as a function of fractional cloud cover, J. Geophys. Res. Atmos.,
1130 111(D9), 2006.

1131
1132 Tarasick, D., Galbally, I.E., Cooper, O.R., Schultz, M.G., Ancellet, G., Leblanc, T., Wallington,

1133 T.J., Ziemke, J., Liu, X., Steinbacher, M. and Staehelin, J.: Tropospheric Ozone Assessment
1134 Report: Tropospheric ozone from 1877 to 2016, observed levels, trends and uncertainties.
1135 Elementa: Science of the Anthropocene, 7, 2019.

1136

1137 Thornhill, G.D., Collins, W.J., Kramer, R.J., Olivie, D., Skeie, R.B., O'Connor, F.M., Abraham,
1138 N.L., Checa-Garcia, R., Bauer, S.E., Deushi, M. and Emmons, L.K.: Effective radiative forcing
1139 from emissions of reactive gases and aerosols—a multi-model comparison. Atmospheric Chemistry
1140 and Physics, 21(2), pp.853-874, 2021.

1141

1142 Veefkind, J.P., de Haan, J.F., Brinksma, E.J., Kroon, M. and Levelt, P.F.: Total ozone from the
1143 Ozone Monitoring Instrument (OMI) using the DOAS technique, IEEE transactions on geoscience
1144 and remote sensing, 44(5), pp.1239-1244, 2006.

1145

1146 Verstraeten, W. W., Boersma, K. F., Zörner, J., Allaart, M. A. F., Bowman, K. W., and Worden,
1147 J. R.: Validation of six years of TES tropospheric ozone retrievals with ozonesonde measurements:
1148 implications for spatial patterns and temporal stability in the bias, Atmos. Meas. Tech., 6, 1413–
1149 1423, <https://doi.org/10.5194/amt-6-1413-2013>, 2013.

1150

1151 Wang, W.C., Zhuang, Y.C. and Bojkov, R.D.: Climate implications of observed changes in ozone
1152 vertical distributions at middle and high latitudes of the Northern Hemisphere, Geophysical
1153 research letters, 20(15), pp.1567-1570, 1993.

1154

1155 Wang, B., R. Wu, K.-M. Lau: Interannual variability of Asian summer monsoon: Contrast between
1156 the Indian and western North Pacific-East Asian monsoons. J. Climate, 14, 4073-4090, 2001.

1157
1158 Wang, H.R., Damadeo, R., Flittner, D., Kramarova, N., Taha, G., Davis, S., Thompson, A.M.,
1159 Strahan, S., Wang, Y., Froidevaux, L. and Degenstein, D.: Validation of SAGE III/ISS Solar
1160 Occultation Ozone Products With Correlative Satellite and Ground-Based Measurements. Journal
1161 of Geophysical Research: Atmospheres, 125(11), p.e2020JD032430, 2020.
1162
1163 Wang, W., Cheng, T., van der A, R.J., de Laat, J. and Williams, J.E.: Verification of the
1164 Atmospheric Infrared Sounder (AIRS) and the Microwave Limb Sounder (MLS) ozone algorithms
1165 based on retrieved daytime and night-time ozone, Atmos. Meas. Tech., 14(2), pp.1673-1687, 2021.
1166
1167 Zhang, L., Jacob, D.J., Liu, X., Logan, J.A., Chance, K., Eldering, A. and Bojkov, B.R.:
1168 Intercomparison methods for satellite measurements of atmospheric composition: application to
1169 tropospheric ozone from TES and OMI. Atmospheric Chemistry and Physics, 10(10), pp.4725-
1170 4739, 2010.
1171
1172 Zhu, T., W. Lin, Y. Song, X. Cai, H. Zou, L. Kang, L. Zhou, and H. Akimoto: Downward transport
1173 of ozone-rich air near Mt. Everest, Geophys. Res. Lett., 33, L23809, doi:10.1029/2006GL027726,
1174 2006.
1175
1176 Ziemke, J.R., Chandra, S. and Bhartia, P. K.: Two new methods for deriving tropospheric column
1177 ozone from TOMS measurements: Assimilated UARS MLS/HALOE and convective-cloud
1178 differential techniques, J. Geophys. Res. Atmos., 103(D17), pp.22115-22127, 1998.
1179

1180 Ziemke, J.R., Chandra, S., Duncan, B.N., Froidevaux, L., Bhartia, P.K., Levelt, P.F. and Waters,
 1181 J.W.: Tropospheric ozone determined from Aura OMI and MLS: Evaluation of measurements and
 1182 comparison with the Global Modeling Initiative's Chemical Transport Model, J. Geophys. Res.
 1183 Atmos., 111(D19), 2006.

1184
 1185 Zhang, R., Wang, H., Qian, Y., Rasch, P.J., Easter, R.C., Ma, P.L., Singh, B., Huang, J. and Fu,
 1186 Q.: Quantifying sources, transport, deposition, and radiative forcing of black carbon over the
 1187 Himalayas and Tibetan Plateau. Atmospheric Chemistry and Physics, 15(11), pp.6205-6223, 2015.

1188

1189

1190

1191

1192

1193

1194

1195

1196 **Table 1.** The mean values and corresponding standard errors of ozone mixing ratio (ppbv) from
 1197 ozonesonde, ozonesonde_(AK) and AIRS over Nainital at six pressure levels and during winter,
 1198 spring, summer-monsoon, autumn are given. The number of ozonesonde flights during four
 1199 seasons are mentioned in the bracket.

Pressure levels	706 (hPa)	496 (hPa)	300 (hPa)	103 (hPa)	29 (hPa)	14.4 (hPa)
ozonesonde	55.1±0.9	54.4±0.7	69.5±2.8	238.8±15.0	4569.3±67.8	7620.6±140.1

Formatted Table

Winter (61)	ozonesonde (AK)	48.6±0.4	55.9±0.6	70.4±1.8	187.3±3.6	5249.1±78.8	8214.9±105.7
	AIRS	46.5±0.3	52.2±0.6	68.7±1.2	354.4±8.4	4428.2±55.8	6616.4±56.0
Spring (72)	ozonesonde	71.6±1.8	70.2±1.5	81.5±2.8	223.9±12.7	4747.0±42.6	8242.3±101.6
	ozonesonde (AK)	58.7±0.7	69.1±1.1	80.3±1.4	221.8±3.6	5137.8±63.4	8784.4±96.6
	AIRS	55.3±0.4	60.7±0.7	78.6±1.0	389.2±6.0	4687.4±38.2	7852.4±97.0
Summer- monsoon (55)	ozonesonde	53.0±2.7	65.1±2.7	82.1±2.5	138.6±3.4	4642.9±26.4	8493.6±91.1
	ozonesonde (AK)	44.1±1.2	62.3±1.7	68.7±1.7	224.3±3.4	5271.3±44.6	9233.8±72.4
	AIRS	48.8±0.5	57.5±0.5	63.6±0.6	267.4±5.5	4710.0±48.2	8333.1±82.5
Autumn (54)	ozonesonde	53.0±1.1	63.8±1.6	72.7±1.6	144.6±6.2	4439.3±28.2	8613.7±77.5
	ozonesonde (AK)	50.4±0.5	61.0±0.8	64.1±0.9	169.0±2.0	5086.3±38.7	9035.8±80.7
	AIRS	46.0±0.3	51.3±0.4	56.9±30.5	241.8±3.6	4635.4±43.9	7984.9±97.6

1200 **Table 2.** Coefficient of determination (r^2) of three IR satellite sensors (AIRS, IASI and CrIS) ozone

1201 retrieval in five broad layers with respect to ozonesonde observations.

	Coefficient of determination (r^2)		
	AIRS	IASI	CrIS
600 - 800 hPa	0.52	0.34	0.09

Formatted Table

300 - 600 hPa	0.44	0.31	0.22
100 - 300 hPa	0.45	0.44	0.45
50-100 hPa	0.87	0.76	0.82
10 - 50 hPa	0.94	0.80	0.94

1202

1203

1204 **Table 3.** Total column ozone (TCO) differences in DU between AIRS, OMI and ozonesonde,
 1205 during twelve months.

TCO Diff. (DU)	Jan	Feb	Mar	Apr	May	Jun	Jul	Aug	Sep	Oct	Nov	Dec
AIRS-OMI	-3.9	2.2	-1.8	13.2	16.7	18	-2.2	17.2	22.1	13.2	0.0	-2.7
AIRS- ozonesonde	-2.1	3.5	6.0	8.1	19.4	11.8	-2.3	22.3	21.6	15.0	5.6	5.2

Formatted Table

1206

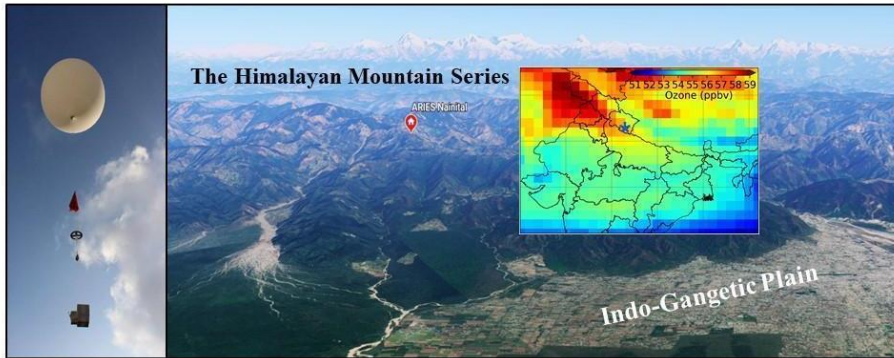
1207

1208

1209

1210

1211



1212

1213 **Figure 1.** Location (red color circle) of the balloon launching site [Map from](#) © Google Earth,
 1214 2021) situated in the Aryabhata Research Institute of Observational Sciences (ARIES) (29.4° N,
 1215 79.5° E, and 1793 m elevation), Nainital in the central Himalaya. The spatial distribution of ozone
 1216 (AIRS) at 500 hPa is also shown over northern India and the location of the site is marked with a
 1217 blue star. A photo of balloon, together with parachute, unwinder, ozonesonde along with GPS-
 1218 radiosonde above the observation site is also shown at the left.

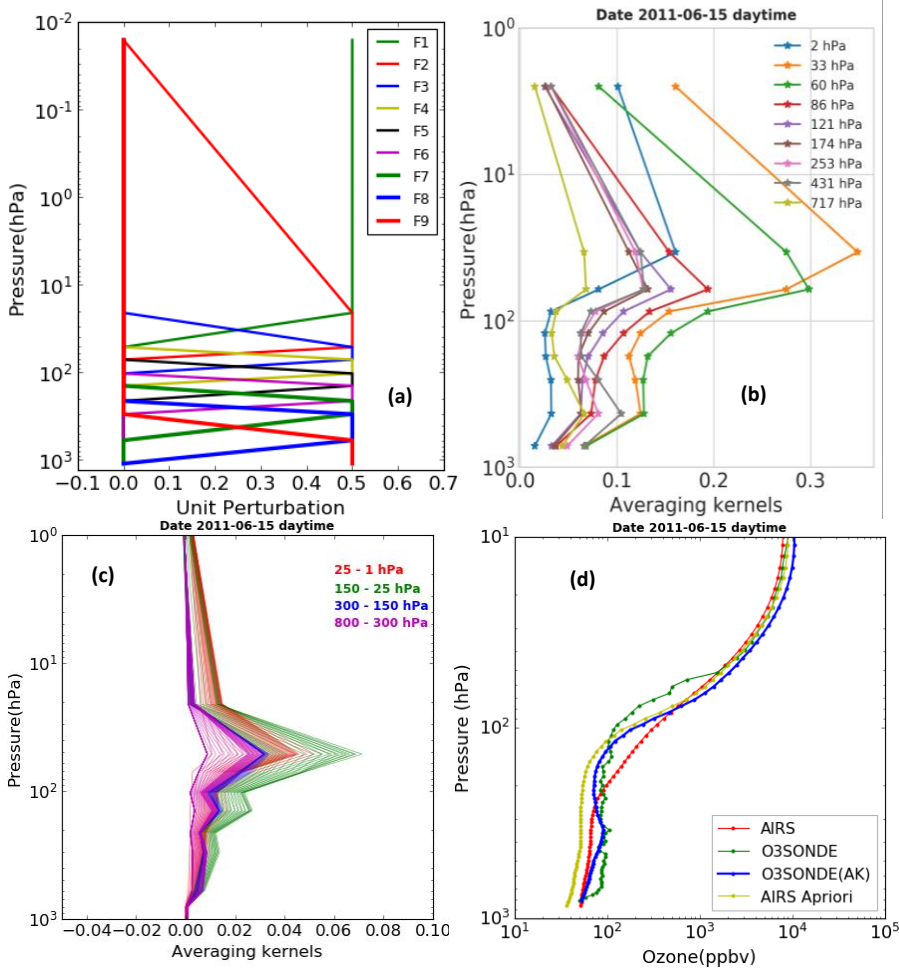
1219

1220

1221

1222

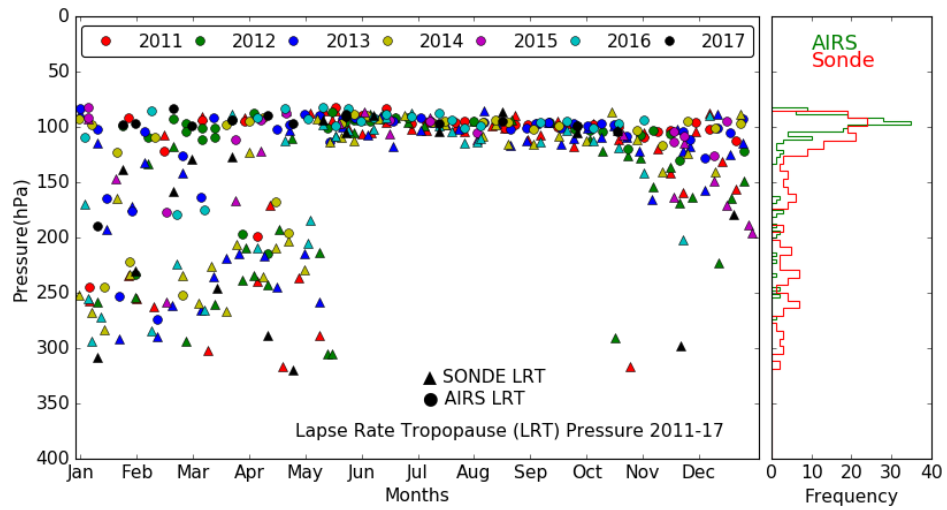
1223



1224

1225
1226

1227 **Figure 2.** (a) Nine trapezoid functions used for ozone retrieval in AIRS-V6. (b) AIRS ozone
 1228 averaging kernel matrix over Nainital at 9 levels vertical grid. (c) Calculated AIRS averaging
 1229 kernel matrices at 100 RTA grids after applying the trapezoid function. (d) An example of ozone
 1230 profiles using different data sets for 15 ~~Jun~~June, 2011 over the observation site.



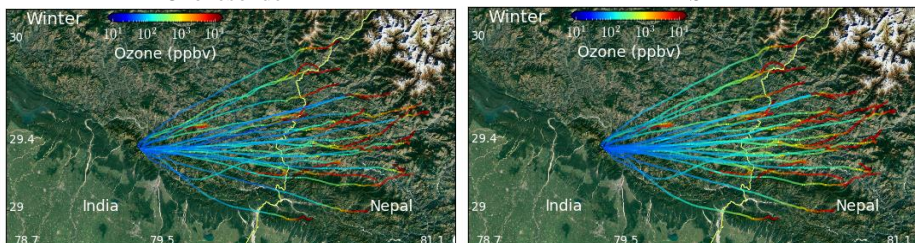
1231
 1232 **Figure 3.** Lapse rate tropopause pressure monthly variation from balloon-borne and AIRS
 1233 observations and respective frequency distributions during 2011 - 2017.

1234
 1235
 1236
 1237
 1238
 1239
 1240
 1241
 1242
 1243

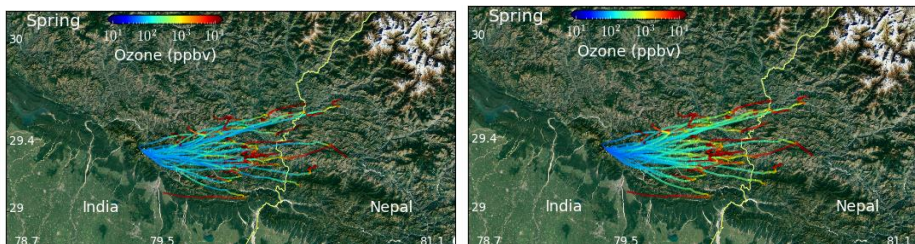
1244

Ozonesonde

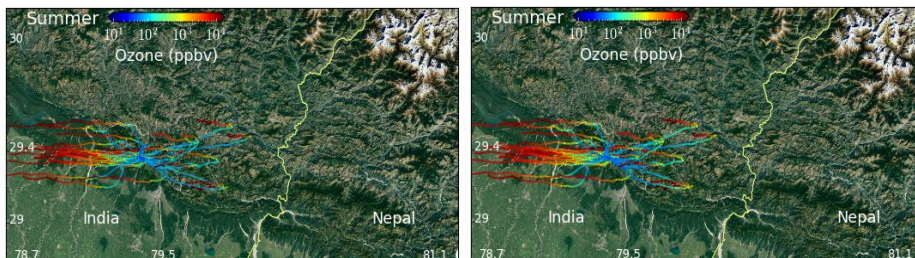
AIRS



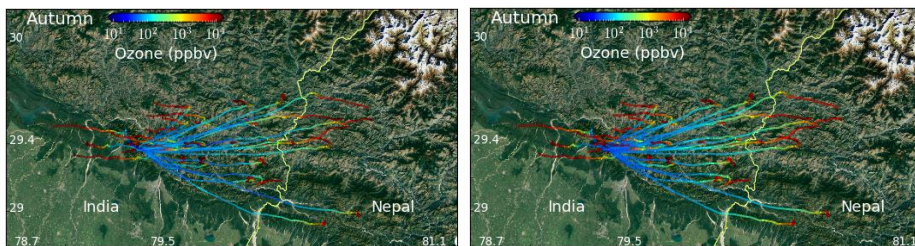
1245



1246



1247



1248

1249

1250

1251

1252

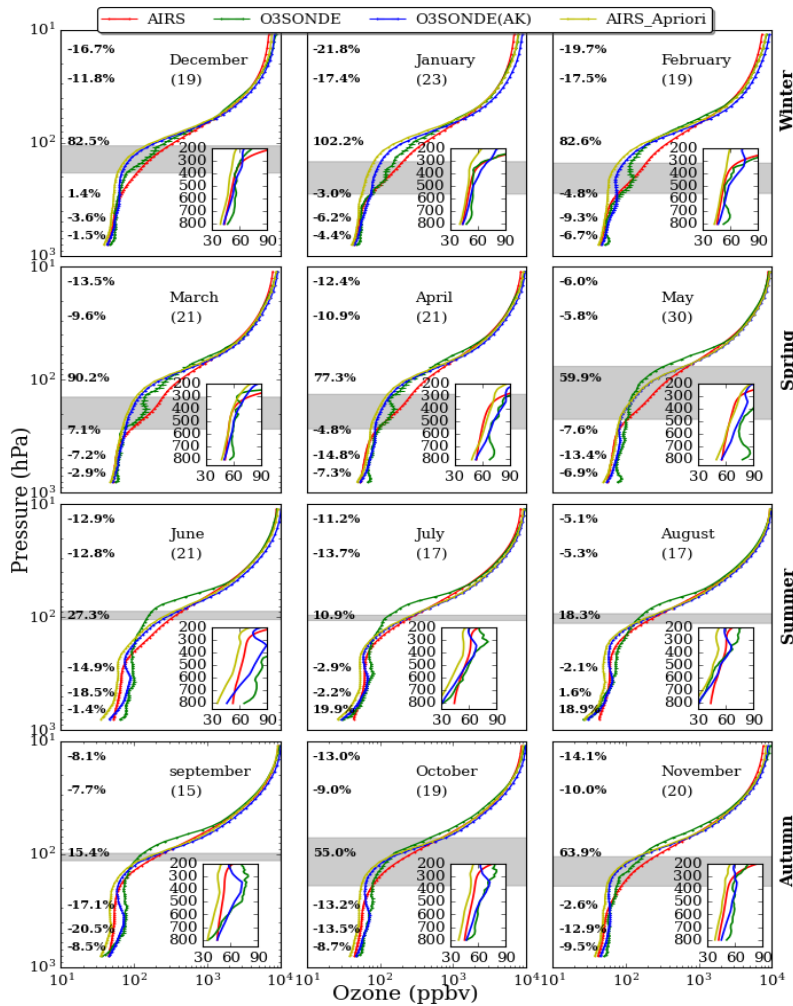
1253

1254

1255

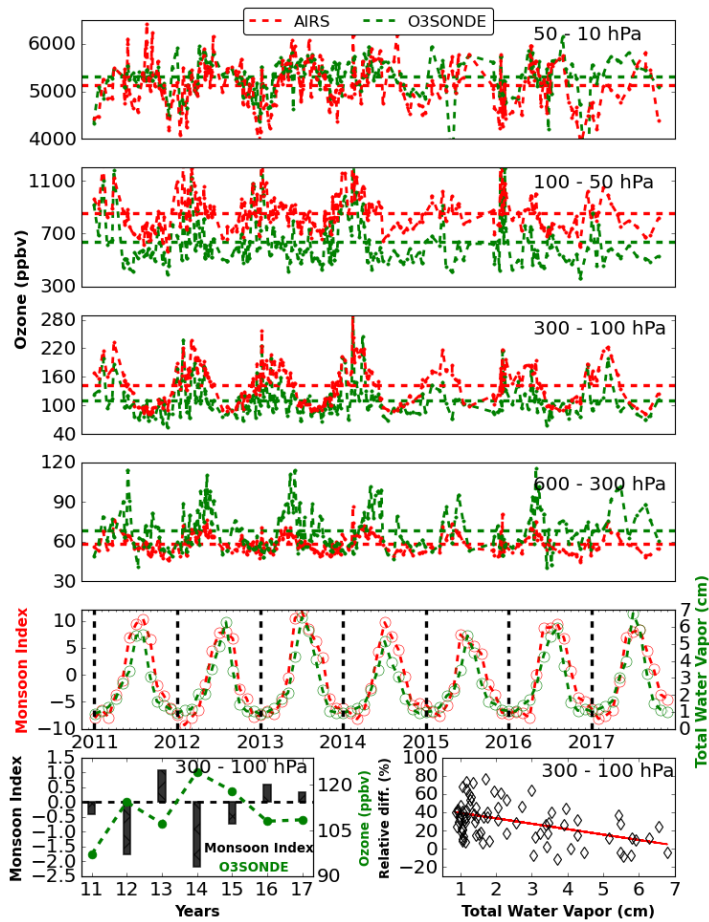
Figure 4. Spatial distribution of ozone using all ozone soundings (left) launched from ARIES, Nainital, India (©Map from Google Earth, 2021), along with the balloon trajectories. Ozone spatial distribution from AIRS (right), following the balloon tracks, is also shown. It could be seen that the balloon reaches Nepal many times in the autumn and winter and autumn seasons.

- Formatted: Font: Times New Roman, 12 pt, Font color: Text 1
- Formatted: Font color: Text 1
- Formatted: Font: Times New Roman, 12 pt, Font color: Text 1
- Formatted: Font color: Text 1, Not Highlight
- Formatted: Font color: Text 1
- Formatted: Font: Times New Roman, 12 pt, Font color: Text 1
- Formatted: Font color: Text 1
- Formatted: Font: Times New Roman, 12 pt, Font color: Text 1
- Formatted: Font: Times New Roman, 12 pt
- Formatted: Font: Times New Roman, 12 pt



1256
 1257 **Figure 5.** Monthly averaged (2011-2017) ozone profiles of ozonesonde, AIRS, ozonesonde (AK)
 1258 and AIRS a-priori over Nainital in the central Himalaya. The percentage difference $[(AIRS -$
 1259 $ozonesonde(AK))/ozonesonde(AK)]*100$ at 706, 496, 300, 103, 29, and 14.4 hPa are also written
 1260 at respective altitudes. The standard error corresponding to each profile is also shown with
 1261 [error bars](#). The number of ozonesonde for different months is written in the bracket and
 1262 grey shaded area shows the tropopause (mean \pm sigma) from balloon-borne observations.

1263
1264



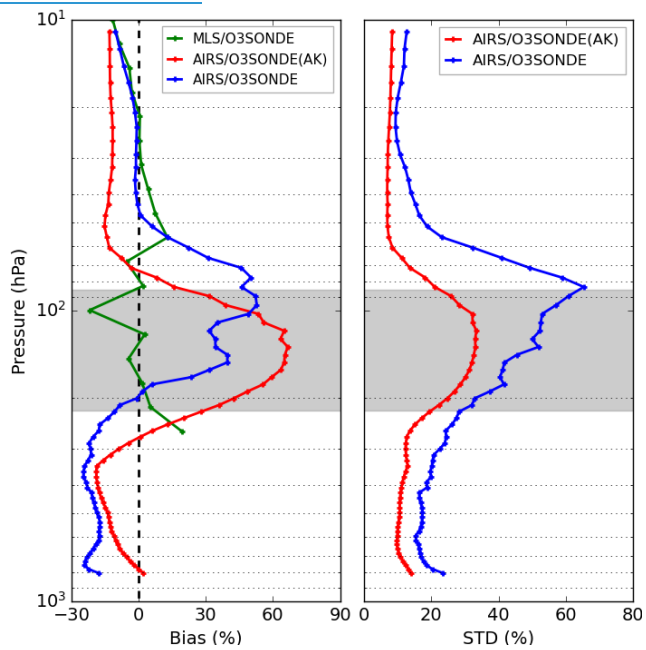
1265

1266 **Figure 6.** Average variations in ozone mixing ratios at four defined layers, characterizing the
1267 middle stratosphere (50 - 10 hPa), the lower stratosphere (100 - 50 hPa), the upper troposphere
1268 (300 - 100 hPa), and the middle troposphere (600 - 300 hPa), respectively. The red and green dash
1269 horizontal lines show the average ozone mixing ratios in the defined layers from AIRS and
1270 ozonesonde, respectively, from 2011 to 2017. The monthly variation of the total column water
1271 vapor (cm) along with the monsoon index is also shown. (left lower most) The yearly average
1272 ozone from ozonesonde and monsoon index (bar plot) for different years and (right (left
1273 lower most) and scattered plot of ozone relative difference (%) [(AIRS-O3SONDE)/O3SONDE]*100,

Formatted: Line spacing: Multiple 1.15 li

1274 with —total water vapor ([right lower most](#)) in the upper troposphere (300 - 100 hPa) [isare](#) also
1275 shown.

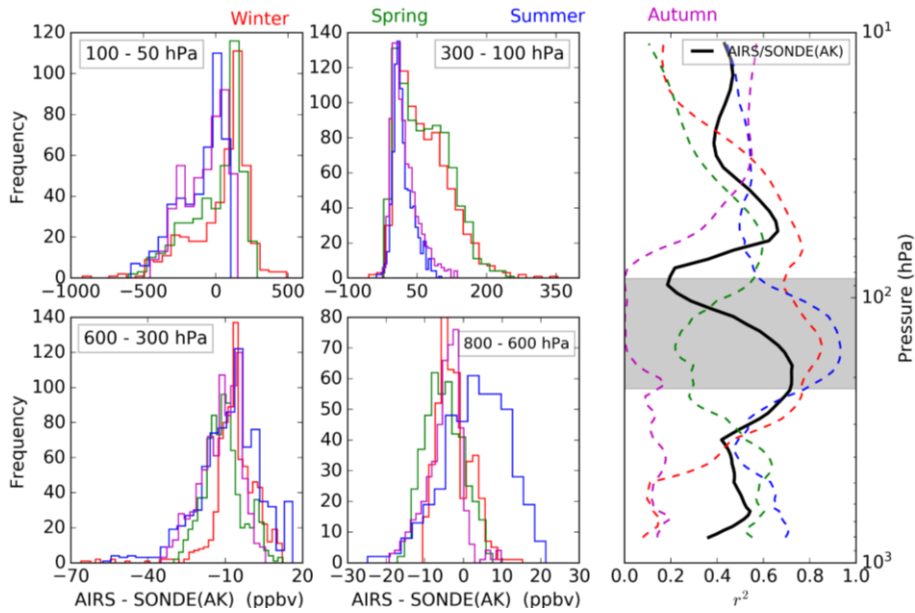
1276



1277

1278 **Figure 7.** Statistical error analysis (Bias and standard deviation) of AIRS retrieved ozone with
1279 ozonesonde and ozonesonde (AK) for collocated data of seven years (2011 - 2017). The Bias
1280 between collocated data of MLS (261 hPa - 10 hPa) and ozonesonde over Nainital during 2011 -
1281 2017 is also shown with the green profile. The grey shaded area shows the tropopause region from
1282 balloon-borne radiosondes observations.

1283

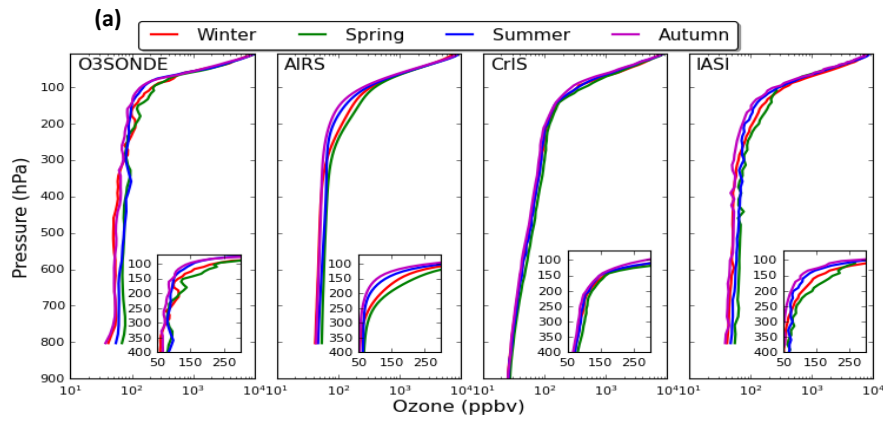


1284
 1285 **Figure 8.** Histogram difference between AIRS ozone and ozonesonde_(AK) in the four defined
 1286 layers. The average correlation profiles between AIRS ozone and ozonesonde_(AK) are shown on
 1287 the right during winter (red), spring (green), summer-monsoon (blue), and autumn (magenta). The
 1288 black line is for the entire data set. The grey shaded area shows the tropopause region from balloon-
 1289 borne radiosondes observations.

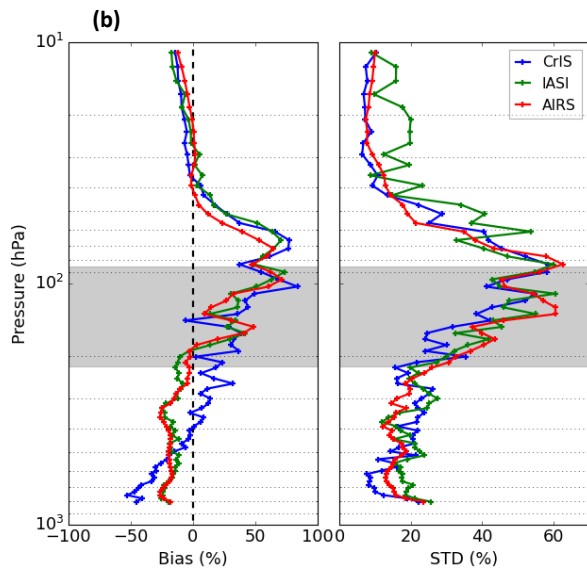
1290

1291

1292



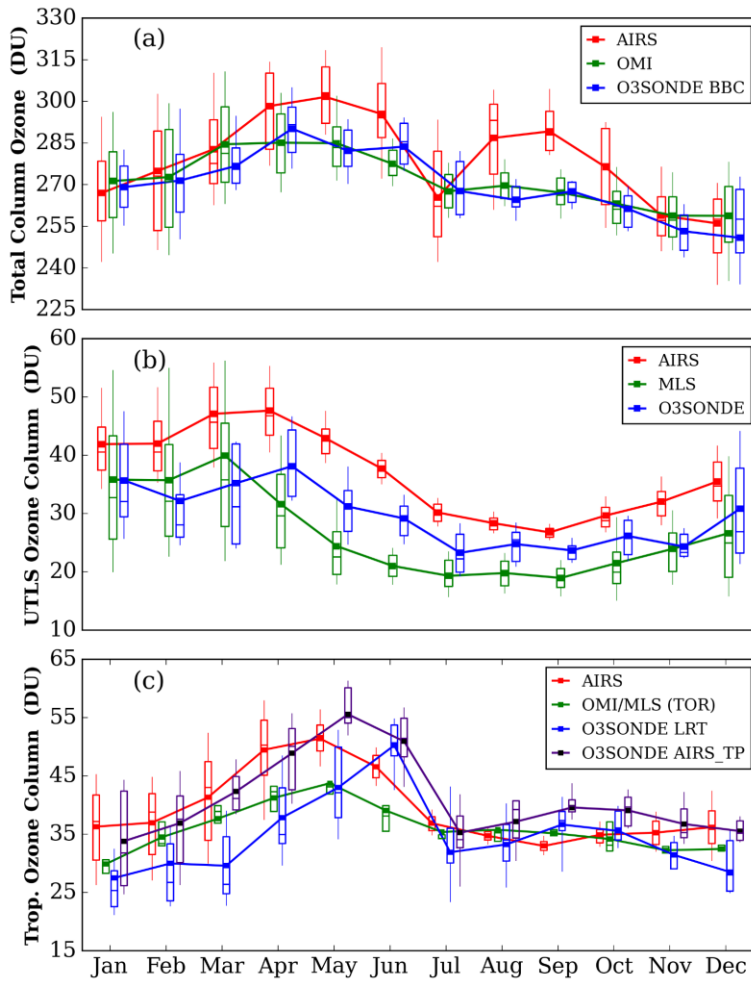
1293
1294



1295

1296 **Figure 9.** (a) Seasonal ozone profiles of three IR satellites (IASI, AIRS, and CrIS) for a smaller
1297 sample size (April 2014 to April 2015). The IASI and CrIS products are generated using the AIRS
1298 heritage algorithm (NOAA) and only zero quality flags (QC=0) of retrieval are used. (b) Statistical
1299 error analysis for the three IR satellites retrieved ozone without applying the averaging kernel
1300 information. The grey shaded area shows the tropopause region from balloon-borne observations.

1301

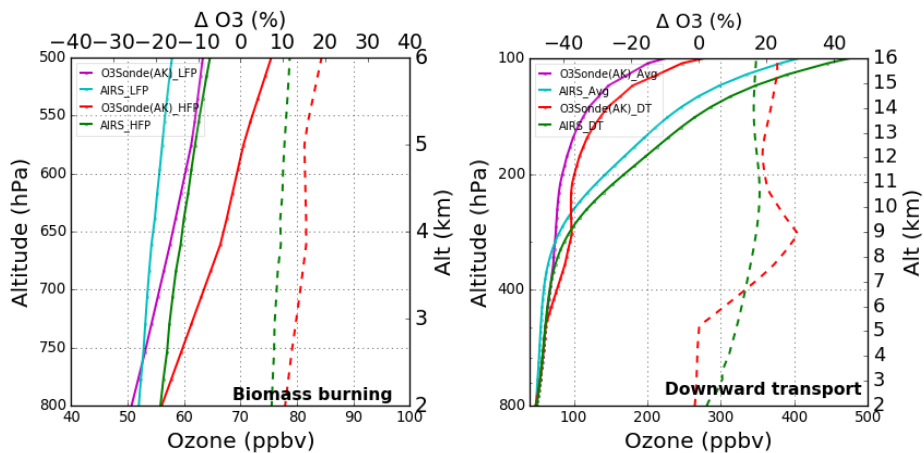


1302

1303 **Figure 10.** (a) Monthly average variations of total column ozone (TCO) for AIRS, OMI, and
1304 ozonesonde (Balloon Burst Climatology) over the central Himalaya for the 2011-2017 period. (b)
1305 Monthly average variation of UTLS ozone column for AIRS, MLS, and ozonesonde, over the
1306 central Himalayas for the 2011-2017 period. (c) Monthly average variations of tropospheric ozone
1307 column of AIRS, OMI/MLS (Tropospheric Ozone Residual), and ozonesonde (LRT — sonde
1308 lapse rate) — over the central Himalayas for the 2011-2017 period. The ozonesonde tropospheric
1309 ozone column is also shown using AIRS tropopause (AIRS_TP). In the box plot, the lower and

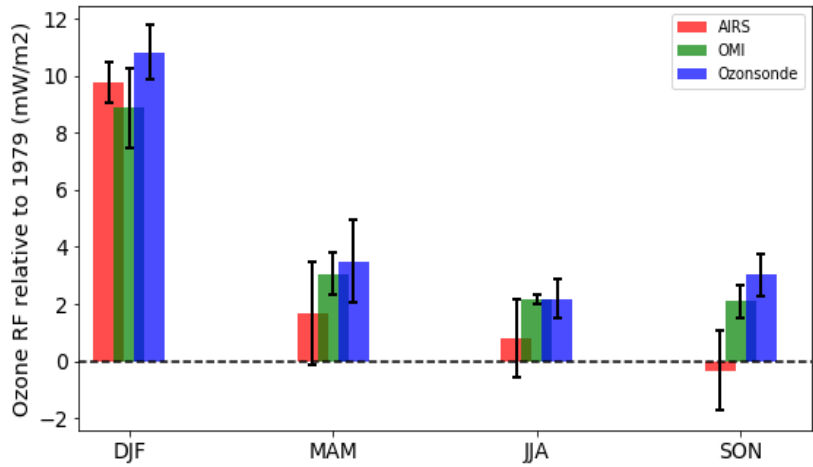
Formatted: Font: Not Bold

1310 upper edges of the boxes represent the 25th and 75th percentiles. The whiskers below and above
 1311 are 10th and 90th percentiles.
 1312



1313
 1314 **Figure 11.** (a) Vertical ozone profiles of AIRS ozone and ozonesonde_(AK) during low fire period
 1315 (LFP) and high fire period (HEP). The solid lines correspond to ozone profiles while the dotted
 1316 lines show a percentage increase in ozonesonde (red) and AIRS (green) profiles during biomass
 1317 burning events. (b) Vertical ozone profiles of AIRS ozone and ozonesonde_(AK) during events of
 1318 downward transport. The dotted line shows ozone enhancement during downward transport
 1319 events.

1320
 1321
 1322



1323
 1324 **Figure 12.** Seasonal average ozone UV radiative forcing (RF) relative to 1979 as calculated from
 1325 ozonesonde, OMI, and AIRS total ozone data for the 2011 - 2017 period. Spreads correspond to
 1326 one standard deviation.
 1327